Irradiation Creep in Graphite

Reactor Concepts RD&D

Dr. Rick Ubic

Boise State University

In collaboration with:

Idaho National Laboratory

Brian Robinson, Federal POC
Will Windes, Technical POC

NEUP Nuclear Energy University Programs

U.S. Department of Energy

Table of Contents ii

Background

Carbon

Crystallographic units of carbon can exist in four different forms: amorphous, turbostratic, pyrolytic, and graphitic (carbon nanotubes are essentially a three-dimensional arrangement of graphene sheets). As expected, amorphous carbon has no identifying microstructural characteristics and is often the first form of carbon to grow in many processing procedures. Graphite is the highly ordered, yet highly two-dimensional, form of graphite which is stable at room temperature but which commonly requires high-temperature post-processing to form. Turbostratic carbon is intermediate between graphite and amorphous carbon.[1] It is built up by nano-scale imperfect graphene layers, arranged almost parallel to one another, but with some disorder,[2] causing interplanar spacings to be greater than in ideal graphite. Indeed, the d_{002} value measured by x-ray diffraction (XRD) is traditionally used to estimate the graphitization degree of carbon, which typically increases with processing temperature. Pyrolytic carbon is a material similar to graphite, but with some covalent bonding between its graphene sheets as a result of imperfections in its production. It is generally produced by heating a hydrocarbon nearly to its decomposition temperature and allowing the graphite to crystallize.

Nuclear grade graphite

Due to its excellent thermo-mechanical and fast-neutron moderation properties, graphite is commonly used as a moderator and structural component in gas-cooled nuclear reactors; however, its anisotropic response to neutron displacement damage due to its close packed crystal structure requires the use of specially manufactured "nuclear" grades of graphite to achieve the desired component lifetimes.[3]

The performance and lifetime of nuclear graphite are closely related to the irradiation environment and are dramatically affected by the specifics of the particular graphite: manufacturing process, graphitization temperature, composition (amount of coke, filler, *etc.*), and geological origin. Several common forms of nuclear grade graphite exist, including Pile grade A (PGA), Pile Grade B (PGB), and Gilsocarbon. PGA graphite was used in early gas-cooled reactors like the Magnox series in the UK and contains filler particles derived from the petroleum industry.[4] These particles tend to have an elongated, needle-like shape that preferentially align with the extrusion axis (Fig. 1a). As the crystallites within the filler particles are also preferentially aligned, the bulk material has anisotropic mechanical properties. PGB is similar but has a lower density and higher neutron capture cross section. Gilsocarbon was later developed for advanced gas-cooled reactors and uses a filler obtained from naturally occurring asphalt called Gilsonite, the coke from which produces spherical, onion-like filler particles that have no preferential alignment (Fig. 1b). Consequently, Gilsocarbon is a near-isotropic polycrystalline graphite with a microstructure composed of spherical coke filler particles embedded in a coal–tar pitch matrix, which is graphitized, with around 20% porosity generated via the different stages of the manufacturing process.[6,7]

In all nuclear graphite there are different scales of porosity, including large gas-evolution pores, calcination cracks, and microporosity formed during cooling from graphitization temperatures often referred to as Mrozowski cracks.[8]
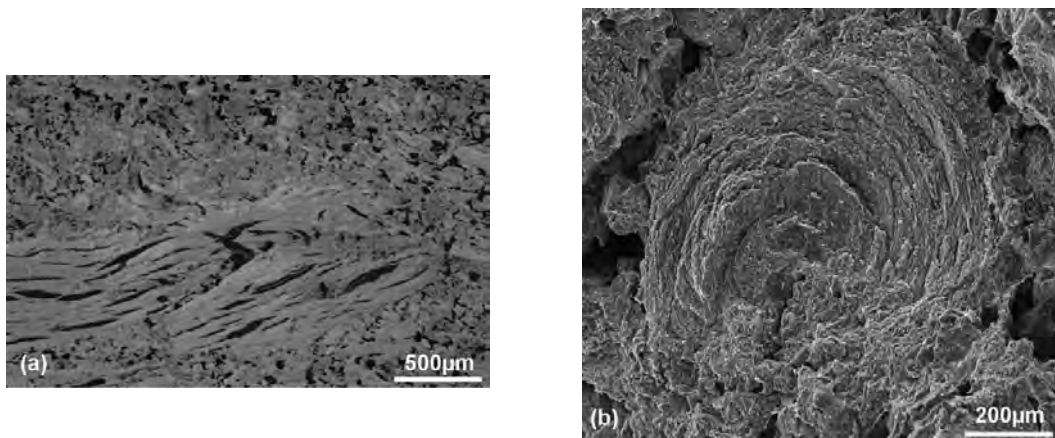
Fig. 1   Nuclear grade graphite. (a) Pile grade A and (b) Gilsocarbon.[5]

Use of nuclear graphite in reactors

Graphite is currently used as a structural material in core designs where the fuel is dissolved in molten fluoride salt and contained inside channels within the graphite; and graphite or pyrolytic carbon is used in the coating of particle fuels in gas-cooled reactors to both contain the fission products and transmit the heat. It is also a leading candidate core material for the extreme operating temperatures envisioned for Generation IV gas-cooled reactor concepts like the very high temperature reactor (VHTR) and the molten salt reactor (MSR),[3] but may also find uses in the CO_2-cooled gas fast reactor (GFR) if some of the technical issues can be resolved.

During operation in carbon dioxide cooled reactors, nuclear graphite is subjected to fast neutron irradiation and radiolytic oxidation which, over time, significantly increases its porosity and adversely affects the mechanical properties. Specifically, irradiation damage from fast neutrons creates lattice defects leading to changes in physical and mechanical properties and the accumulation of stresses. The inevitable gradients in both neutron flux and temperature (exacerbated by a decrease in thermal conductivity with irradiation) produce internal stresses which, under irradiation, can be relived by plastic deformation. Radiolytic oxidation is caused by the reaction of oxidizing species from the carbon dioxide coolant gas, produced by gamma radiation, with the graphite. Such oxidation reduces the density and hence the moderating capability of the graphite, but also reduces the strength and hence integrity of the core.[9]

Recently, Berre *et al.*[10] used x-ray tomography to develop a modeling technique for the microstructures of Gilsocarbon and examined the effects on mechanical properties. Joyce *et al.*[11] found that high strain ratio areas in the microstructure of Gilsocarbon tended to be associated with porosity, both in the matrix and within the coarse filler particles; however, the correlation was not perfect and strain localization was not observed at all pores. The fracture path passed through significant strain localizing features in most, but not all, cases.

Wen *et al.*[12] studied the microstructures of the binders in both Gilsocarbon and PGA. They observed a variety of carbon structures, including a well-graphitized structure, nanosized graphite particles, quinoline insoluble (QI) particles (Fig. 2), chaotic structures and non-graphitizing carbon. QI particles were observed on the surface and inside mesophase spheres. The aggregation of QI particles on or near the surface of mesophase spheres appeared to have a significant influence on the development of the mesophase structure, resulting in refinement of the mesophase spheres before their coalescence. The chaotic structure, which is turbostratic and isotropic, may have developed from the isotropic pitch remaining between mesophase spheres.   The non-graphitizing carbon consisted of flat and curved single-layer graphene

2

fragments with a size typically less than 1 nm. The formation of the various structures in the two graphites was attributed to the different pitches used in their manufacture.
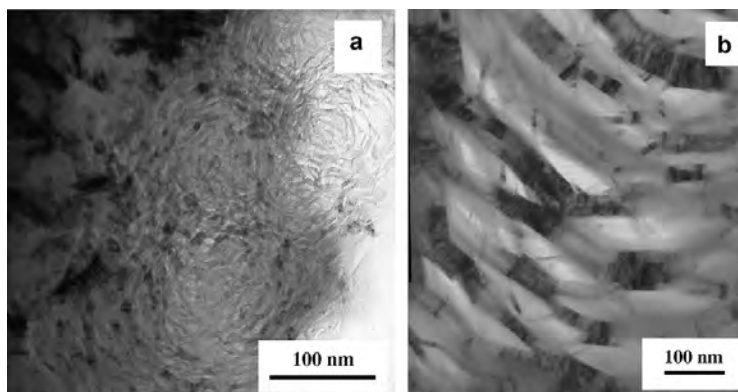

Fig. 2   (a) TEM image from Gilsocarbon showing agglomeration of four QI particles;
(b) higher magnification image showing the structure of QI particles.[12]

Agglomerations of small, spherical particles were also observed within the binder (Fig. 2a). Such particles have previously been observed in the binder of pitch-bonded graphites and have been referred to as rosettes.[13]   They have also been observed in carbon blacks produced from elemental carbon vapor generated by decomposition of SiC powder.[14]

Irradiation creep
As deformation by slip without cracks generally requires at least five independent slip systems,[15] and graphite can only slip along two directions parallel to its basal plane,[16] microcracks would tend to develop under strain in normal conditions; however, irradiation can induce strains via other mechanisms.

The residual strain in graphite due to irradiation under stress consists of three parts: a stress-independent irradiation-induced dimensional change, plastic deformation associated with an increase in elastic modulus, and irradiation creep.[17]   The apparent increase in modulus can be explained by assuming that plastic deformation is prevented by the pinning of dislocations by radiation defects. The irradiation creep component is actually essential, as it allows for the dissipation of stresses built up by gradients in neutron flux and temperature.[18]   Traditionally, the observed creep strain has been separated into a primary reversible component and a secondary irreversible one, both proportional to stress and the unirradiated elastic compliance.

A number of theories exist to explain the mechanism of irradiation creep, including grain-boundary sliding, restraint of crystallite *c*-axis growth, migration of point defects down stress gradients, yield of crystallites due to radiation-induced internal stresses, and pinning-unpinning of basal plane dislocations. While none of these theories has so far satisfactorily explained all of the experimentally-observed observations, the dislocation pinning-unpinning model results in the best overall agreement. According to this model,[19] the creep rate should be inversely proportional to modulus, in agreement with observations. Graphite normally contains a high density of basal-plane dislocations which are kept immobile by pinning points. Neutron irradiation creates clusters of interstitial atoms which act as new pinning points. Under these conditions, dislocations can move through the lattice under applied stress and cause basal shear, with the dislocation velocity proportional to the stress. It follows that the creep rate should be inversely proportional to the pinning-point density.

3

Motivation

There are currently 433 commercial nuclear reactors in the world which collectively provide about 16% of the world's electricity needs.[3] Most of these reactors are of the Generation II (water cooled) type developed in the 1970s. The technology of the Generation III reactors of the last 10 years is essentially the same; however, the next-generation reactors must have enhanced power conversion efficiencies and the ability to produce hydrogen, best accomplished with high-temperature gas-cooled systems.

In order for the Generation IV nuclear plants (the so-called Next Generation Nuclear Plants or NGNP) to operate more efficiently, economically, and safely, several advanced designs have been proposed[20] which will require them to run at higher temperatures with higher radiation fluxes and more corrosive coolants. The principal challenge to the success of these advanced reactor concepts is the development of high-performance materials.[21-29] In particular, it is the reactor core and vessel containment that pose the unique materials challenges for nuclear power. The common feature of all advanced designs is high operating temperature (compared to current Generation II light water reactors) and most will also involve very high neutron dose rates. These challenges will place increased emphasis on strength, creep, and creep-fatigue behavior of the materials used.

Nearly all of the major graphite research programs (NGNP, British Energy, PBMR) are performing, or planning to perform, irradiated graphite creep experiments in order to establish irradiation creep rates for a number of nuclear grade graphite types. For the most part these are engineering studies that focus on the specific creep rates and creep behaviors of the graphite types in question. Less emphasis is placed upon understanding the fundamental mechanisms behind irradiation creep of graphite. While understanding these mechanisms is understood to be important, establishing the specific creep rates for specific graphite types to predict the core behavior during reactor operations has been considered a more appropriate action for the relatively quick development times needed for these programs.

The Advanced Graphite Creep (AGC) experiment for the US-NGNP research program will provide creep rate and behavior for a number of production-ready graphite types. Irradiation creep rate, effects of irradiation creep on material properties, and irradiation-induced changes to the graphite microstructure (*i.e.*, pore structure) are being investigated to some extent; however, limited or no research is being performed on some fundamental aspects related to irradiation behavior of graphite. Specifically, there have been no thorough studies addressing the lack of data on creep mechanisms within graphite (*i.e.*, dislocation movement or lack thereof), the lack of experimental data for irradiation dimensional changes, or the inter-relationship between these important mechanisms. This research will focus on these fundamental issues and provide experimental data to validate or invalidate current theories held by the research community.

Scope and Aims

An understanding of the underlying mechanism(s) of irradiation creep in graphite material is required to correctly interpret experimental data, explain micromechanical modeling results, and predict whole-core behavior. The proposed project will focus on experimental microscopical data to demonstrate the mechanism of irradiation creep. High-resolution transmission electron microscopy should be able to image both dislocations in graphite as well as, for example, irradiation-induced interstitial clusters which pin them. The power of the technique notwithstanding, the goal remains a challenging one and will require considerable effort on the part of the team.

A postdoctoral research assistant, with the aid of an undergraduate, will conduct the experimental work. Samples of virgin nuclear graphite will first be prepared and characterized on the nano scale in a transmission electron microscope (TEM). Additional samples will be irradiated to varying degrees at the Advanced Test Reactor (ATR) facility (beam time to be applied for separately) and similarly characterized. A similar experiment was recently conducted at the ATR on Magnox graphite. The exact form of graphite in this work will be defined by the NGNP program. Microstructures and crystal defects will be recorded and a mechanism for irradiation creep suggested based on the results. In addition, the purchase of a tensile holder for TEM will allow the in-situ observation of creep behavior on the microstructure and crystallographic defects for the first time.

There are two institutions collaborating on this project. Co-PI *B* will supervise bulk deformation studies on graphite and coordinate experiments in the Advanced Test Reactor (ATR). His/her lab has facilities to heat specimens to 2400°C in a variety of environments, including controlled concentrations of $CO-CO_2$. The PI will oversee the microscopical investigation of graphite samples including the *in-situ* deformation studies. Co-PI *A* will provide samples as well as facilitate experiments and irradiated-sample preparation in dedicated labs. Further intellectual contributions from colleagues at the University of Manchester (formerly UMIST) will provide the team with a strong basis on which to build. The unique strengths of the individual project members and their facilities will enable the team will operate in a truly synergistic way. Each team member possesses specific expertise and capabilities, and the overall program will be organized so as to take best advantage of these capabilities whilst simultaneously encouraging collaboration in areas of overlap.

References

1. D. V. Badami and G. Kaye, "*The Nature of Turbostatic Carbon*," Carbon, 1 375-375 (1964).
2. B. E. Warren, "*X-ray diffraction in random layer lattices*," Phys. Rev., 59 693-698 (1941).
3. Y. Guérin, G.S. Was, and S.J. Zinkle, "*Materials challenges for advanced nuclear energy systems*," MRS Bull., 34 [1] 10-14 (2009).
4. B.T. Kelly, "*The structure and manufacture of nuclear grade graphite, irradiation damage in graphite due to fast neutrons in fission and fusion systems*," IAEA-TECDOC-1154, IAEA (2000).
5. G. Hall, B.J. Marsden, and S.L. Fok, "The microstructural modelling of nuclear grade graphite," *J. Nucl. Mater.*, 353 [1-2] 12-18 (2006).
6. J.E. Brocklehurst and B.T. Kelly, "Analysis of the dimensional changes and structural changes in polycrystalline graphite under fast-neutron irradiation," *Carbon*, 31 [1] 155-178 (1993).

7. R.E. Nightingale, Nuclear Graphite, Academic Press, London, 1962.

8. S. Mrozowski, "Mechanical strength, thermal expansion and structure of cokes and carbons," p. 31 in *Proc. 1st and 2nd Conferences on Carbon*, Buffalo, NY, Waverly Press (1956).

9. S.B. Grover and M.P. Metcalfe, "*Graphite materials testing in the ATR for lifetime management of Magnox reactors*," INEEL/CON-02-00370 (2002).

10. C. Berre, S.L. Fok, B.J. Marsden, P.M. Mummery, T.J. Marrow, and G.B. Neighbour, "*Microstructural modelling of nuclear graphite using multi-phase models*," J. Nucl. Mater., 380 46-58 (2008).

11. M.R. Joyce, T.J. Marrow, P. Mummery, and B.J. Marsden, "*Observation of microstructure deformation and damage in nuclear graphite*," Eng. Fract. Mech., 75 3633-3645 (2008).

12. K.Y. Wen, T.J. Marrow, and B.J. Marsden, "*The microstructure of nuclear graphite binders*," Carbon, 46 62-71 (2008).

13. S.S. Jones and E.M. Woodruff, "*Microstructure of carbon blacks in pitch-bonded graphites and structural changes produced by gas-graphite oxidation reactions*," Carbon, 9 259–64 (1971).

14. K. Yamada and S. Tobisawa, "*Structure and formation process of carbon blacks formed by decomposing SiC powder using a conically converging shock-wave technique*," Carbon, 27 845–52 (1989).

15. G.I. Taylor, "*Plastic strain in metals*," J. Inst. Metall., 62 307-324 (1938).

16. S. Amelinckx and P. Delavignette, "*Electron optical study of basal dislocations in graphite*," J. Appl. Phys., 31 [12] 2126-2135 (1960).

17. A.J. Perks and J.H.W. Simmons, "*Radiation-induced creep in graphite*," Carbon, 1 [1] 441-449 (1964).

18. B.T. Kelly and T.D. Burchell, "*The analysis of irradiation creep experiments on nuclear reactor graphite*," Carbon, 32 [1] 119-125 (1994).

19. B.T. Kelly and A.J. Foreman, "*Theory of irradiation creep in reactor graphite - dislocation pinning-unpinning model*," Carbon, 12 [2] 151-158 (1974).

20. A Technology Roadmap for Generation IV Nuclear Energy Systems, U.S. DoE Nuclear Energy Advisory Committee and the Generation IV International Forum, GIF-002-00, December 2002, http://gif.inel.gov/roadmap/.

21. D. Butler, "*Energy: Nuclear power's new dawn*," Nature, 429 [20] 238-240 (2004).

22. L.K. Mansur, A.F. Rowcliffe, R.K. Nanstad, S.J. Zinkle, W.R. Corwin, and R.E. Stoller, "*Materials needs for fusion, Generation IV fission reactors and spallation neutron sources - similarities and differences*," J. Nucl. Mater., 329-333 166-172 (2004).

23. T.R. Allen, J.T. Busby, R.L. Klueh, S.A. Malloy, and M.B. Toloczko, "*Cladding and duct materials for advanced nuclear recycle reactors*," JOM, 60 15-23 (2008).

24. B. Raj, M. Vijayalakshmi, P.R.V. Rao, and K.B.S. Rao, "*Challenges in materials research for sustainable nuclear energy*," MRS Bull., 33 327-337 (2008).

25. G.R. Odette, M.J. Alinger, and B.D. Wirth, "*Recent developments in irradiation-resistant steels*," Annu. Rev. Mater. Res., 38 471-503 (2008).

26. J.L. Boutard, A. Alamo, R. Lindau, and M. Rieth, "*Fissile core and tritium-breeding blanket: structural materials and their requirements*," C. R. Phys., 9 287-302 (2008).

27. S.J. Zinkle and N.M. Ghoniem, "*Operating temperature windows for fusion reactor structural materials*," Fusion Eng. Des., 51-52 55-71 (2000).

28. K. Ehrlich, J. Konys, and L. Heikinheimo, "*Materials for high performance light water reactors*," J. Nucl. Mater., 327 140-147 (2004).

29. F. Carré, C. Renault, P. Anzieu, Ph. Brossard, P. Yvon. *Outlook to France's R&D Strategy on Future Nuclear Systems*, Research Reactor Fuel Management Conference (RRFM 2007), Lyon, France (March 2007).

Technical Summary of work Accomplished

Simulated neutron-induced damage process in nuclear graphite

Summary
Atomic-level processes involved in the swelling and crack-closing of nuclear-grade graphite under electron irradiation have been observed in real time using transmission electron microscopy. Noise-filtered lattice images show the formation of vacancy loops, interstitial loops, and resulting dislocations with unprecedented clarity.   The dislocation dipoles formed via vacancy loops were found to undergo climb resulting in the formation of extra basal planes. Concurrent studies via electron-energy loss spectroscopy (EELS) showed a reduction in the atomic density because of the breakage of hexagonal carbon rings. The formation of new basal planes via dislocation climb in addition to the bending/breaking of basal planes leads to swelling and closing of micro-cracks.

Experimental details
TEM samples of commercial nuclear-grade graphite, NBG-18 (supplied by SGL group, Germany), were prepared by conventional sample preparation techniques. Disks with 3 mm diameters were cut from the as-received bulk graphite and further thinned mechanically to approximately 100 µm.   An ion slicer (EM09100-IS, JEOL), purchased with an NEUP infrastructure award, was used to achieve the final electron transparency.   Compared to conventional ion-milling techniques, the ion slicer is known to produce minimal beam damage in specimens. In-situ electron irradiation studies were performed at room temperature using a 200 kV JEOL-2100 high resolution transmission electron microscope (TEM) fitted with an EELS spectrometer (Enfina 1000, Gatan). Since the irradiation-induced processes were rapid, they were captured on video for later slowing. The noise reduction of the videos was achieved via notch-pass filtering of fast Fourier transforms using a MATLAB® code developed at Boise State University.

Results
Fig. 1 shows the microstructure filler and binder regions in NBG-18.   The complex microstructure of nuclear graphite arises from the manufacturing process which involves mixing coke filler particles (petroleum or coal tar) with a binder (pitch). The micro-cracks seen in Fig. 1a are formed due to the anisotropic thermal-expansion coefficient, which leads to de-lamination when the graphite billets cool from high graphitization temperatures. These micro-cracks play a vital role in determining the magnitude of irradiation-induced swelling as they can accommodate crystalline swelling that occurs at lower irradiation doses. Fig 1b shows a region of binder which is embedded with rosette-like particles which result from the graphitization of solid quinoline-insoluble (QI) particles made up of high molecular-weight aromatic molecules present in the pitch binder [1].

The electron irradiation-induced microstructural changes, in particular the closing of micro-cracks were studied in the filler particles where they are long and lenticular in nature and are believed to have the most influence on irradiation-induced property changes. Fig 2 shows the effect of intense electron irradiation on the micro-cracks. The electron beam was focused (~5 x 10^{21} electrons/cm^{2}s) and positioned to cover the center of the micro-crack with an initial width at the center of about 20 nm. With increased irradiation, the graphite showed significant swelling and the crack closed completely after only 20 s irradiation time.   The dosage in terms of displacement per atom (dpa) was estimated to be approximately 1 dpa. A significant decrease in the diffraction contrast in the irradiated area as seen in Fig. 2b indicates a decrease in the crystallinity of the graphite. Such behavior has also been reported elsewhere [2].
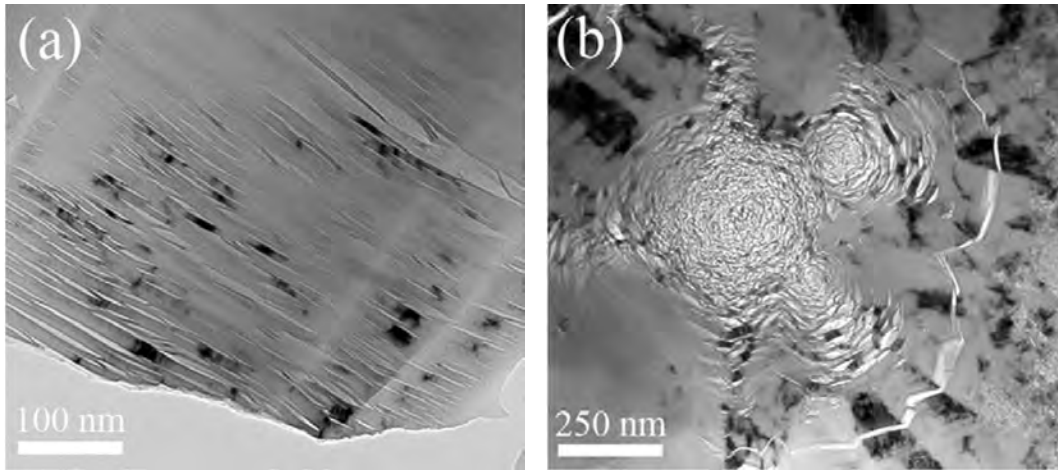
Fig. 1   Bright field TEM micrographs showing the microstructure of NBG-18 grade nuclear graphite recorded from (a) filler and (b) binder region
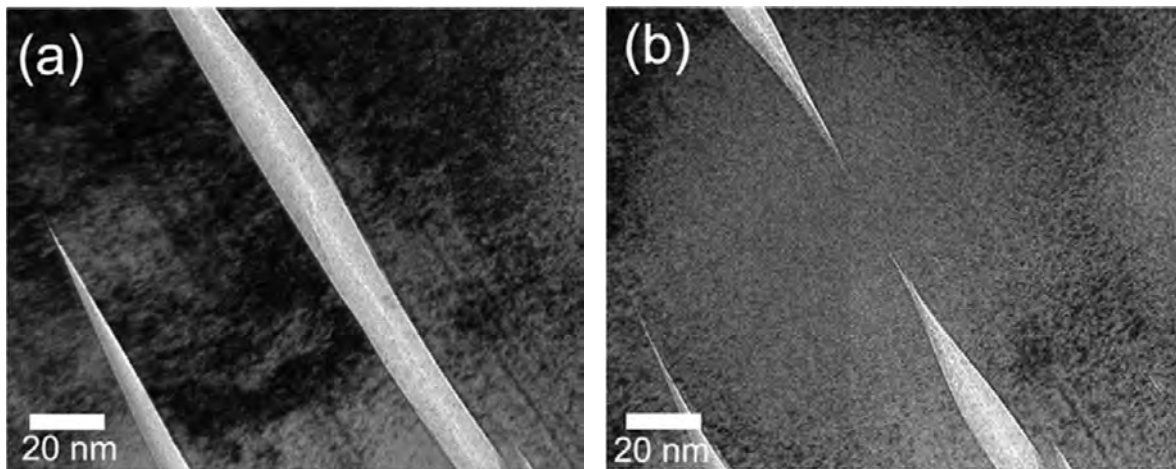

Fig. 2   Bright-field TEM micrographs showing the effect of electron irradiation on nuclear graphite; (a) shows a micro-crack present in the as-prepared sample and (b) the same crack after ~1 dpa irradiation.

Fig. 3a–c shows lattice images recorded along [100] depicting the sequential changes in the (001) basal planes associated with swelling and crack-closing induced by electron irradiation. The crack with a width of ~20 nm seen in Fig. 3a completely disappeared (Fig. 3c) due to swelling of the crystallite from either side. It is clearly shown that, with the increased electron dose, the graphite basal planes lose their long-range order with the formation of breaks and bends, eventually leading to randomization.   The shape of the 002 reflections in the corresponding fast Fourier transform (FFT) patterns changed from spots to arcs (Fig. 4), indicating fragmentation and rotation of the basal planes which only retain a layered structure locally within a scale of few nanometers (Fig. 3). The average (002) inter-planar spacing was estimated to increase approximately 13% from 3.6 nm to 4.2 nm.

During the initial stages of electron irradiation, the nucleation of numerous dislocation dipoles was observed, the concentration of which increased with increasing dpa. These dislocations were created by the formation of vacancy loops (Fig. 3a inset).
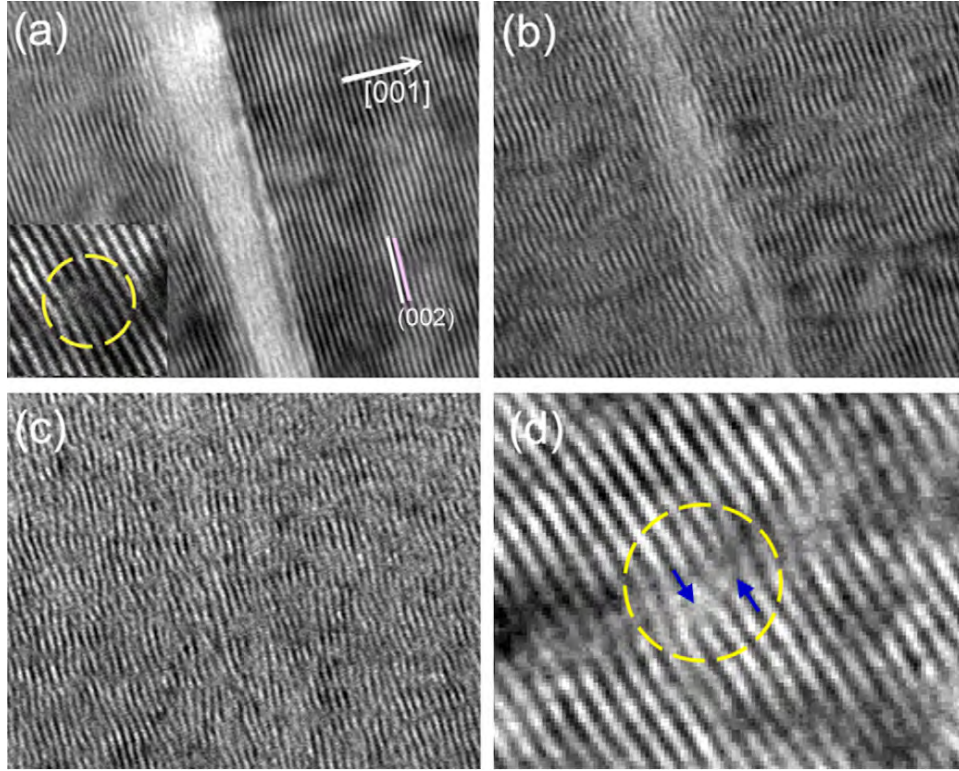
Fig. 3 High-resolution TEM images showing the effect of electron irradiation on the graphite lattice. Images (a) – (c) were recorded sequentially from as-prepared, ~0.5 dpa, and ~1 dpa irradiated samples. The inset in (a) shows the nucleation of vacancy loops. The image in (d) is a close-up view of the lattice recorded after ~0.25 dpa showing the creation of dislocation dipoles, one of which is indicated within a dashed circle.
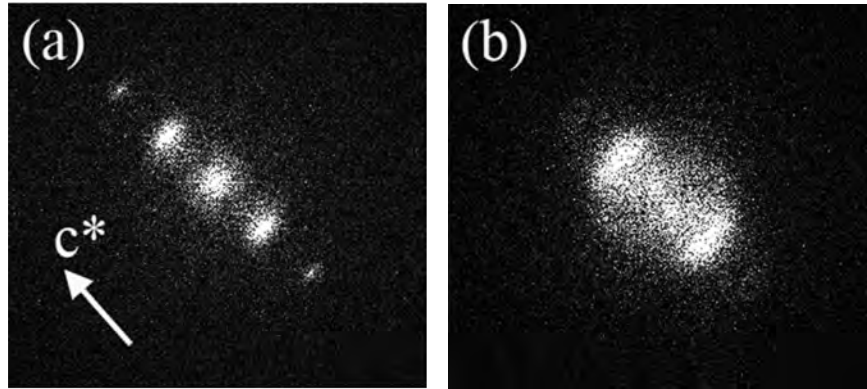
Fig. 4 FFT of high-resolution TEM images recorded from (a) as-prepared and (b) ~1 dpa irradiated samples

These images are highly noisy due to the fast scan rate used to capture the rapid changes in the lattice structure. Fig. 5a shows a noise-filtered image which clearly shows the nucleation of a vacancy loop (marked with arrows) which leads to the formation of a set of edge dislocations with opposite Burgers vectors as shown in Fig. 5b. These two snapshots were captured within 1 s of each other. Fig 5b also shows the nucleation of more vacancy loops. It should be noted that the ballistic displacement of carbon atoms under intense electron irradiation results in high concentrations of vacancies and interstitials. According to Amelinckx [3], these dislocation loops, formed due to the precipitation of vacancies, are known to contain a low-energy single

9

stacking fault (one layer of rhombohedral stacking) with a Burgers vector of $\frac{1}{2}<001>+\frac{1}{3}<\overline{2}10>$. Subsequent snapshots (Fig. 5c-d) show that these dislocations move via positive climb. Fig 5c clearly shows the growth of the incomplete planes, marked with arrows, which effectively results in the formation of an extra basal plane. In the case of neutron irradiation, it has been assumed from TEM observations of irradiated graphite [4] that the formation of interstitial loops is the reason for the swelling along the c-axis, but the images of electron-irradiated graphite presented here show that extra basal planes can form without the initial formation of interstitial loops. It should be noted that the whole process is dynamic with numerous dislocations being constantly created and annihilated with only a few dislocations undergoing climb.
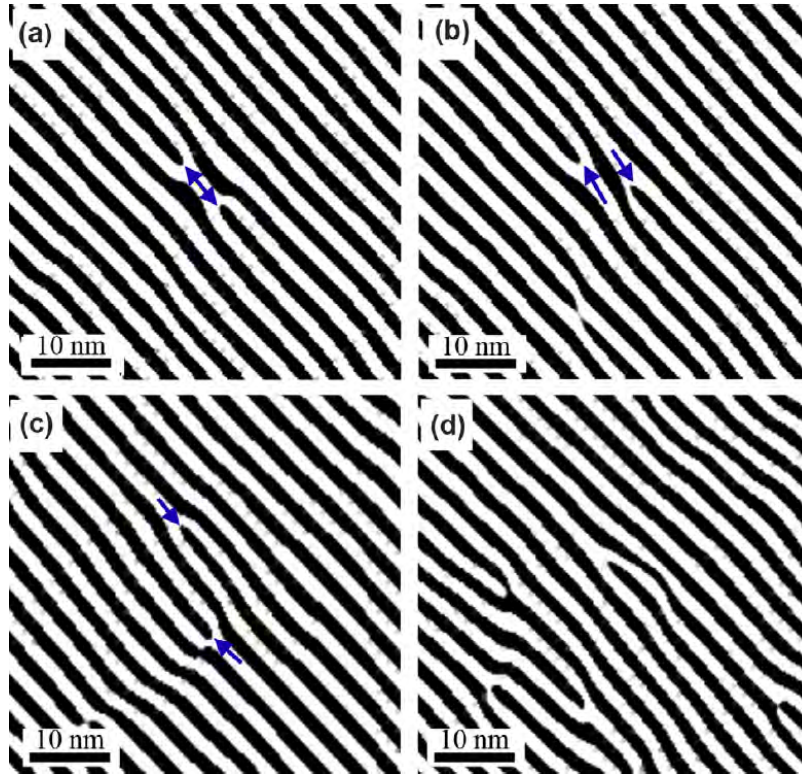

Fig. 5 Noise-filtered TEM images showing the formation of dislocation dipoles via vacancy loops; (a) the nucleation of a vacancy loop (~0.25 dpa) dissociating itself into (b) a set of dislocations with the incomplete planes marked with arrows; (c) the growth of the incomplete planes via positive climb; and (d) the accumulation of several dislocations at higher irradiation doses resulting in disordering of the graphite lattice. The distance between two black fringes corresponds to the (002) interplanar spacing (~0.36 nm).

Apart from vacancy loops, the formation of interstitial loops (precipitation of interstitials) was also observed (Fig. 6). Fig. 6a shows the bending of planes outward indicative of compressive stress exerted by an interstitial cluster even though the loop is not resolvable by the Fourier analysis. According to Muto and Tanabe [5], the interstitial loops must be larger than half the sample thickness in order to be visible in TEM images. A subsequent snapshot recorded after 1 s of irradiation (Fig 6b) shows a more fully grown interstitial loop with a lateral length of about 5 nm. Most of the loops observed in this work were of similar size. The interstitial loops of sufficient size are considered to introduce a new *c* layer in the otherwise *ab* stacking of trigonal graphite. This type of interstitial loop, also referred to as prismatic dislocation loops, are essentially partial dislocations with a Burgers vector of ½[001] [6]. These interstitial loops were

found to be highly unstable and destroyed by further electron irradiation. With the increased irradiation, the concentration of dislocations also increased, leading to an increase in the concentration of broken graphite layers, eventually leading to more randomization (Fig. 5d).
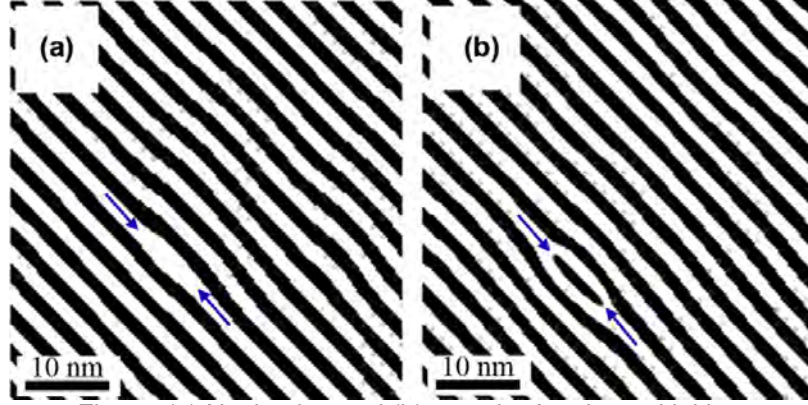

Fig. 6   (a) Nucleation and (b) growth of an interstitial loop

In order to obtain a better understanding of the implications of the electron-irradiation damage on atomic bonding, EELS was used to study the changes in the bonding environment associated with breakage and randomization of the graphite layers. Fig. 7 shows the low-loss and core-loss EELS spectra recorded for as-prepared and ~1 dpa irradiated graphite corresponding to the microstructures shown in Fig. 3a and c. The low-loss spectrum shown in Fig. 7a has two prominent features, a π plasmon peak around 6 eV and $\pi + \sigma$ plasmon peak around 25 eV. The $\pi + \sigma$ plasmon peak showed a shift towards lower energies with an increase in the irradiation damage. The energy shift was 1.9 eV for 1 dpa irradiation. A shift towards lower energies indicates a reduction in valance electron density which could be indicative of a volume expansion or of structural transitions such as the formation of non-six-sided carbon rings [7]. It should be noted that there is a weak π plasmon peak still present even after 1 dpa irradiation indicating that the layered structure associated with π bonds is retained, although largely aperiodic, even at this stage of irradiation, confirming the microstructural observations (Fig. 3).

From the peak position (E_p) of the $\pi + \sigma$ plasmon peak, the change in the valence electron density (n_e) of the graphite was calculated using a relationship based on the quasi-free electron model [8],

$$n_e = \frac{E_p \varepsilon_0 m^*}{\hbar e^2}$$

where m^* is the effective mass of electrons (for graphite, $m^* = 0.87 m_e$, where m_e is the free-electron mass [9]) and ε_0 is the permittivity of free space (8.854×10^{-12} F/m). The mass density can then be estimated from n_e using the atomic mass of carbon and the number of valance electrons per carbon (4). This method of calculating mass density has been used and verified previously [9,10]. From Fig. 7a, the densities of the as-prepared and ~1 dpa irradiated graphite have been estimated to be 2.28 g/cm^3 and 1.96 g/cm^3, respectively; an average fall in density of about 16%. It should be noted that the density of the as-prepared graphite is essentially the theoretical density of single-crystalline graphite (2.26 g/cm^3), which gives validation to this method.
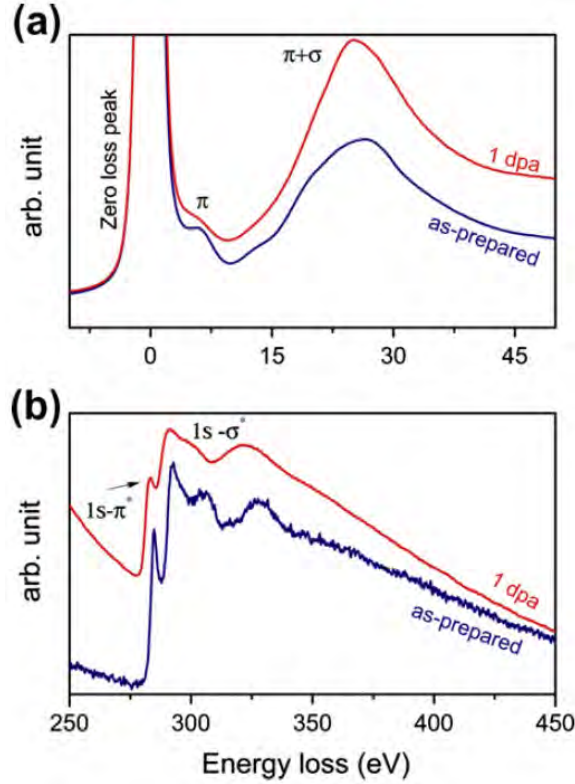
Fig. 7 (a) Low-loss and (b) core-loss EELS spectra of the graphite recorded from the as-prepared and ~1 dpa irradiated graphite

The K-edge core-loss spectra for the corresponding doses are shown in Fig. 7b. The spectra have two main features: a peak at ~285 eV and a maximum with extended fine structures at ~290 eV which are attributed to 1s-π^* and 1s-σ^* electronic transitions, respectively. It can be seen that the fine structure in the σ^* peak disappeared with the formation of a broad peak, which is indicative of the formation of fullerene-like structures [11]. This change indicates the deterioration of the long-range periodicity within the basal plane due to the formation of non-hexagonal atomic rings, which agrees with the previously calculated reduction in density. Apart from destroying the long-range ordering, the dislocation dipoles are also believed to aid the formation of so-called bucky onions [12] because the dipoles induce curvature of the basal planes, which is consistent with the formation of bends and curves in the present case and may explain the changes observed in the EELS spectra. Recently, Chuvlin *et al.* [13] have shown fullerene formation in real time from a graphene sheet under electron irradiation. Also, the accumulation of interstitial carbon atoms themselves can induce local buckling of basal planes by forming cross-links between the basal planes.

Initially, the formation and growth of new interstitial planes as a result of accumulation of displaced carbon atoms was considered to be the sole reason for the macroscopic swelling of graphite along the *c*-axis; but there was no clear microstructural evidence, creating doubt as to this hypothesis [6]. In this work, clear evidence for the formation of interstitial loops at room temperature has been shown; however, the interstitial loops were found to be highly unstable and few in number, therefore unlikely to significantly contribute to the observed swelling. The swelling along the *c*-axis and the closing of micro-cracks is instead mainly due to the new basal planes being introduced by the positive climb of dislocation dipoles created via vacancy loops. The dislocation climb involves the migration and effective accumulation of carbon atoms along

the *c*-axis leaving behind a high concentration of vacancies, the condensation of which on free surfaces might be a reason for the simultaneous *a*-axis shrinkage. In addition, the significant reduction in density observed even at 1 dpa shows the increase in the open nature of the lattice. As the dislocation dipoles increase in concentration, they introduce breaks, bends and curls in the basal planes, leading to the destruction of the lattice ordering and resulting in a more open structure, as proposed by Niwase [14] and observed here experimentally via the increase in the interplanar (001) spacing visible in lattice images and the decrease in density demonstrated via EELS.

References

1.	K.Y. Wen, T.J. Marrow, B.J. Marsden, Carbon 46 (2008) 62.
2.	K.Y. Wen, J. Marrow, B. Marsden, J. Nucl. Mater. 381 (2008) 199.
3.	S. Amelinckx, P. Delavignette, Phys. Rev. Lett. 5 (1960) 50.
4.	P.A. Thrower, W.N. Reynolds, J. Nucl. Mater. 6 (1963) 221.
5.	S. Muto, T. Tanabe, Phil. Mag. A 76 (1997) 679–690.
6.	R.H. Telling, M.I. Heggie, Phil. Mag. 87 (2007) 4797.
7.	M. Takeuchi, S. Muto, T. Tanabe, S. Arai, T. Kuroyanagi, Phil. Mag. A 76 (1997) 691.
8.	R.F. Egerton, Electron Energy-Loss Spectroscopy in the Electron Microscope, Plenum, New York, 1986.
9.	A.C. Ferrari, A. Libassi, B.K. Tanner, V. Stolojan, J. Yuan, L.M. Brown, S.E. Rodil, B. Kleinsorge, J. Robertson, Phys. Rev. B 62 (2000) 11089.
10.	R. Haerle, E. Riedo, A. Pasquarello, A. Baldereschi, Phys. Rev. B 65 (2001) 045101.
11.	M. Takeuchi, S. Muto, T. Tanabe, H. Kurata, K. Hojou, J. Nucl. Mater. 271 (1999) 280.
12.	K. Niwase, Mater. Sci. Eng. A 400 (2005) 101.
13.	A. Chuvilin, U. Kaiser, E. Bichoutskaia, N.A. Besley, A.N. Khlobystov, Nature Chem. 2 (2010) 450.
14.	K. Niwase, Phil. Mag. Lett. 82 (2002) 401.

Microstructural characterization and pore structure analysis of nuclear graphite

Summary
Graphite will be used as a structural and moderator material in next-generation nuclear reactors. While the overall nature of the production of nuclear graphite is well understood, the historic nuclear grades of graphite are no longer available. The microstructural characteristics of filler particles and macro-scale porosity in virgin nuclear graphite grades of interest to the Next Generation Nuclear Plant program were investigated. Optical microscopy was used to characterize the morphology of filler particles as well as the arrangement of shrinkage cracks. Computer-aided image analysis was applied to optical images to quantitatively determine the variation of pore structure, area, eccentricity, and orientation within and between grades. The overall porosity ranged between ~14% and 21%. A few large pores constitute the majority of the overall porosity. The distribution of pore area in all grades was roughly logarithmic in nature. The average pore was best fit by an ellipse with aspect ratio of ~2. An estimated 0.6–0.9% of observed porosity was attributed to shrinkage cracks in the filler particles. Finally, a preferred orientation in the porosity was observed in all grades.

Experimental details
Nuclear graphite grades IG-110, PGX, NBG-18, and PCEA were selected for characterization. NBG-18 and PCEA were chosen because of the Next Generation Nuclear Plant (NGNP) program's interest for high irradiation dosage regions of the Very High Temperature Reactor (VHTR) [2,3]. IG-110 is a fine-grained historical reference grade which is currently being used in the HTTR and HTR-10 and is in many ways similar to IG-430, also a high-dose candidate for the VHTR. PGX is a candidate grade for low dosage regions of the VHTR reactor.

Sample preparation
Samples prepared for optical microscopy and pore analysis were approximately 0.2 cm thick and had an observable surface of approximately 2.25 cm^2. To strengthen the graphite samples internally and prevent degradation of pore walls and surface flow during polishing, samples were impregnated with epoxy resin and allowed to cure for 24 h. The graphite samples were hand-polished with successively finer SiC abrasive paper to a final grit of 1200. Next, samples were placed without additional weight into a vibratory polisher and allowed to polish for 3 h in a 0.3 μm SiC water-based suspension. Upon completion, samples were cleaned with deionized water to remove any remaining SiC abrasive.

Optical microscopy and image analysis
Optical microscopy was carried out using a bench-top Olympus BX51 Optical Microscope. Programming and code execution for pore identification and analysis were carried out using MATLAB® (MathWorks, USA) and its image processing toolbox. The bright-field micrographs used for pore analysis were taken at a magnification of 5x. The pixel resolution of micrographs used for pore analysis was ~0.7 μm. The smallest pores identified were in the range of 5 μm^2; however, sample artifacts of similar sizes were also observed. To distinguish between porosity and small artifacts, higher magnifications were needed; therefore, the minimum pore size measured in this work was arbitrarily set to 12.5 μm^2. It was not necessary to use higher magnification in the case of such pores. Original micrographs were formatted as 24-bit color files as shown in Fig. 1a for PGX graphite. Once uploaded to MATLAB they were converted to 8-bit grayscale images. The color-to-grayscale transformation was accomplished by eliminating the hue and saturation information while retaining the luminance of the color image (Fig. 1b). Fig. 1c shows a histogram of the grayscale image in Fig. 1b, in which two distinct peaks can be seen near 0 and 220 corresponding to the porosity and graphitic material, respectively. Each graphite grade produced a nearly identical histogram. Contrast stretching was applied to all

grayscale images. The reference points for contrast stretch were approximately 50 and 220. The lower reference of ~50 was chosen because it corresponded well with a local minima, yet it was still well within the range of what could easily be determined as porosity. The upper reference was chosen to correspond with the peak intensity of the polished graphitic material. Contrast stretching was performed to increase the sensitivity of the threshold parameter used for converting the images to the binary image matrices (Fig. 1d). Typical values for the threshold parameter (allowable values are normalized between 0 and 1 over the 8 bit range of 0–255) were 0.45 for PGX, NBG-18, and PCEA and 0.37 for IG-110.
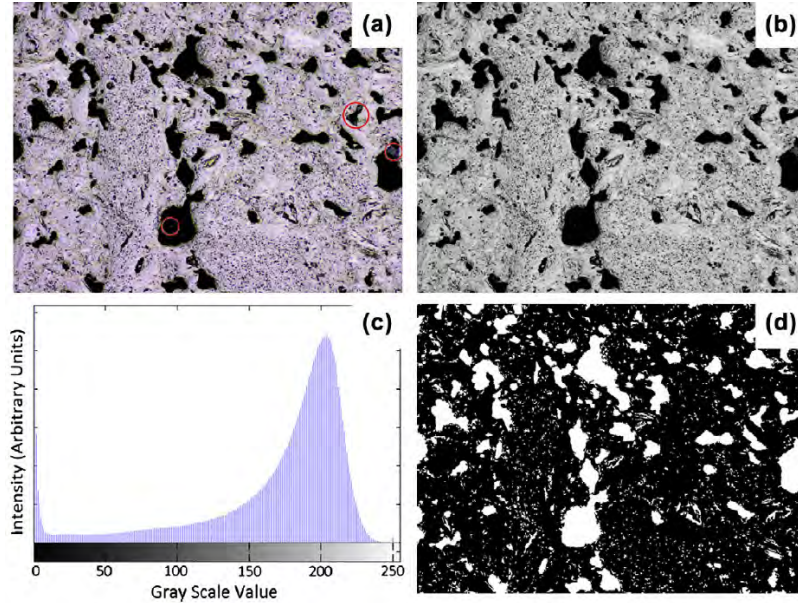

Fig. 1. Basic image processing flow: (a) original colored micrograph, (b) grayscale micrograph of (a) with hue and saturation removed but luminance retained, (c) histogram of (b) prior to contrast stretching and thresholding, (d) final binary image which is run through the connective-components algorithm to extract quantitative pore data.

Two additional processing steps were used between converting to a binary image and data collection. The first was removal of small pores of area less than 25 μm^2 using morphological opening. Next was the removal of small "islands" such as those circled in Fig. 1a. This step involved the use of a morphological flooding algorithm. These "islands" were removed under the assumption that they were either loose graphite fragments that had become lodged in pores or artifacts of the 3D nature of the pores which were not directly in the polished plane of the sample.

To identify each pore and its respective pixels from the binary matrix, a connective-components algorithm was applied with neighboring pixels defined as $N_4(p)$, the left, right, top, and bottom neighbor pixels [15]. Additional algorithms were used to extract the number of pixels (pixel area), the centroid coordinates within the matrix, perimeter, and orientation of each pore. Ellipses were used to provide a quantitative estimate of pore shape. The ellipse with the same normalized second central moment as the pore was used. The eccentricity (*e*), major axis length (*M*), minor axis length (*m*), and orientation of the major axis with respect to the horizontal image plane was extracted for each pore. The eccentricity of an ellipse is related to the major (*M*) and minor (*m*) axis lengths as

$$e = \frac{\sqrt{M^2 - m^2}}{M}$$

As such, eccentricity is defined between the degenerate cases of 0 and 1, where 0 is a circle and 1 is a line.

Results

Filler particle size analyses
The nature of the coke is integral to the development of the filler microstructure in nuclear graphite. As seen in Figs. 2–5, the shape of the filler particles varies from acicular to spherical. The shape of filler particles in general is a function of the coke's innate ability to align its rudimentary graphitic crystallites during calcination. Graphite with a petroleum-based coke tends to have anisotropic, acicular particles resulting from a high degree of alignment of rudimentary crystallites. On the other hand, pitch cokes are in general more isotropic and spherical in nature as a result of their smaller degree of rudimentary crystallite alignment. A summary of the size and shape of the filler material for each grade is given in Table 1.

Table 1   Measurements of observed filler material. MAL = major axis length; σ = standard deviation; AR = aspect ratio.

Grade	Sample size	Mal mean[a] (μm)	Mal σ (μm)	AR mean[a]	AR σ
PGX	624	92 ± 7	85	3.1 ± 0.1	1.6
PCEA	320	126 ± 10	94	2.6 ± 0.2	1.6
NBG-18	300	360 ± 25	217	~1	–
IG-110	625	27 ± 2	22	3.9 ± 0.2	2.4

[a] Means are two-sided confidence intervals, α = 0.05.

Fig. 2.   Optical micrographs of IG-110 graphite: (a) typical bright-field micrograph showing filler, binder, and porosity; (b) bright-field micrograph showing magnified view of the highlighted region in (a); (c) bright field micrograph of filler where the bright regions running along the length of the filler particle are shallow shrinkage cracks; and (d) dark-field micrograph. P = Porosity, F = Filler, B = Binder, C = Shrinkage crack.

The filler observed in IG-110, a fine grained, petroleum based, nuclear graphite appears acicular (Fig. 2). The mean length of filler observed was 27 ± 2 µm with a standard deviation (σ) of 22 µm. This value agrees well with the average length given by the manufacturer (20 µm). The mean aspect ratio observed for IG-110 filler is 3.9 ± 0.2, σ = 2.4. Observed in Fig. 2c are shrinkage cracks that run parallel to the major axis of the particle. These cracks form during calcination as a result of the establishment of rudimentary basal planes of carbonaceous material, strongly suggesting that the *c*-direction of the graphitic crystallites is aligned with the minor axis of the particles.

The filler in PGX is also petroleum-based graphite. It is acicular, much like IG-110, but significantly larger in size (Fig. 3). PGX filler particles are approximately three times larger than those in IG-110, with a length of 92 ± 7 µm and σ = 85 µm. The aspect ratio of PGX filler was 3.1 ± 0.1 with σ = 1.6. Shrinkage cracks in PGX are more numerous and of greater thickness than those observed in IG-110.

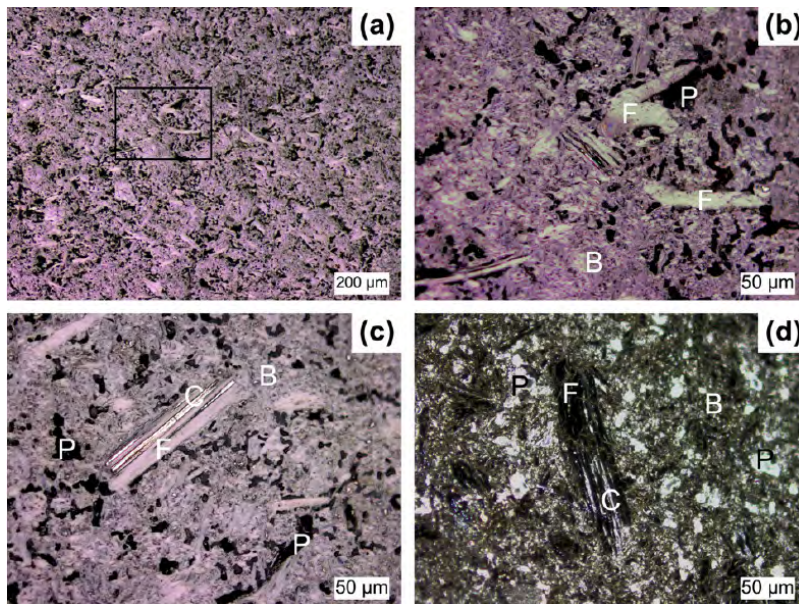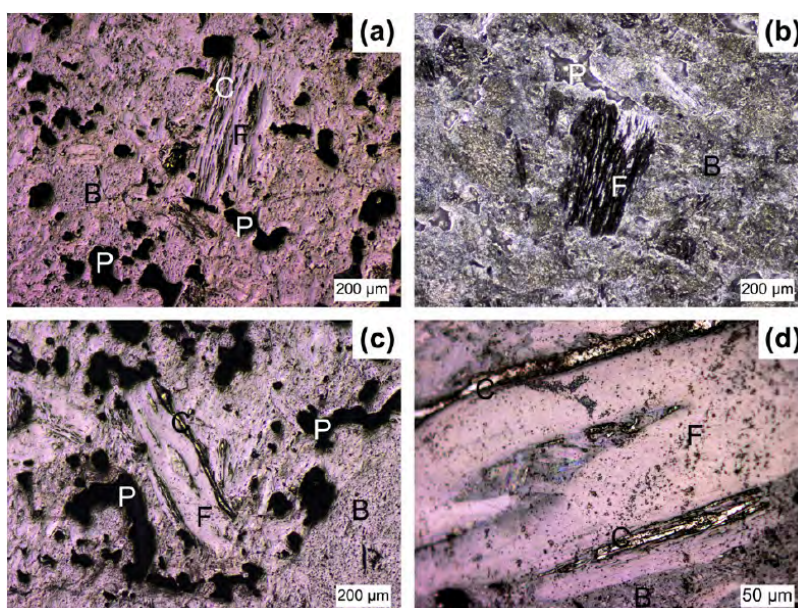

Fig. 3. Optical micrographs of PGX graphite: (a) typical bright-field micrograph showing filler, binder, and porosity; (b) dark-field micrograph of filler in binder matrix; (c) bright-field micrograph of filler with long shrinkage cracks running parallel to the particle long axis; and (d) bright-field micrograph magnifying (c). P = Porosity, F = Filler, B = Binder, C = Shrinkage crack.

The filler material in NBG-18, a pitch-based graphite, appears to be spherical in nature (Fig. 4). The mean particle size observed was 360 ± 25 µm with σ = 217 µm. The maximum particle size observed was 1796 µm which corresponds roughly with the manufacturer's stated maximum particle size of 1600 µm. The roughly 200 µm difference may in part be due to the difficultly in defining an exact particle boundary. The nearly spherical nature of the NBG-18 filler material suggests a relatively low degree of crystalline alignment within the particles. The crystallites in the center of the particles, in general, appear to be small and randomly oriented (Fig. 4b). Those toward the particle exterior appeared larger, with their long axes aligned with the particle circumference.

The shrinkage cracks in NBG-18 vary greatly in size. Many of the larger shrinkage cracks, as observed in Fig 4a and b, are oriented with their long axis approximately tangential to the particle's radial direction. Further magnification of the filler particles in Fig. 4a, c and d show the

orientation of the small shrinkage cracks in the interior of the filler particle and near the perimeter respectively. The small shrinkage cracks toward the center of the filler particles appear to be randomly oriented, while those near the perimeter of the particle appear to be oriented similar to the larger shrinkage cracks.
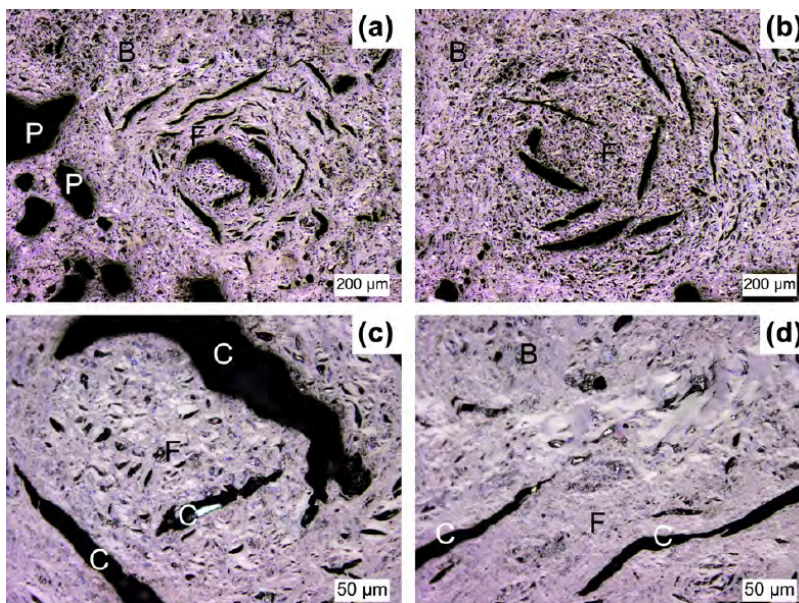

Fig. 4. Optical micrographs of NBG-18 graphite: (a) bright-field micrograph showing filler particle, binder, and porosity; (b) bright-field micrograph of filler surrounded by binder matrix; (c) bright-field micrograph magnifying the inner region of filler particle in (a); and (d) bright-field micrograph magnifying the outer perimeter of filler particle in (a). P = Porosity, F = Filler, B = Binder, C = Shrinkage crack.

PCEA, a petroleum-based graphite, had a wide geometrical variation in observed filler particles (Fig. 5). Approximately 70% of filler is acicular in shape. The acicular particles had a mean length of 137 ± 12 µm with σ = 88 µm. The mean aspect ratio of the acicular particles is 3.2 ± 0.2 with σ = 1.4. The acicular particles in PCEA are slightly larger than those in PGX but have a nearly identical aspect ratio. The spherical filler particles in PCEA had a mean diameter of 99 ± 21 µm with σ = 102 µm. PCEA filler material appears to have varying degrees of crystalline alignment. The spherical filler particle shown in Fig. 5c appears to have crystalline alignment similar to that observed in the center of NBG-18 filler particles (Fig. 4). These crystallites are relatively small and have a random orientation. The crystallites observed in Fig. 5b appear to have a high degree of crystalline alignment similar to that observed in PGX particles (Fig. 3). The shrinkage cracks observed in PCEA were relatively narrow compared to cracks observed in NBG-18, and the orientation appeared random for small shrinkage cracks. Large shrinkage cracks appeared to have a preferred orientation along the particles' long axes for acicular particles (Fig. 5a and d). For spherical particles, the shrinkage cracks were aligned with one another but not along any particular axis of the filler particle.
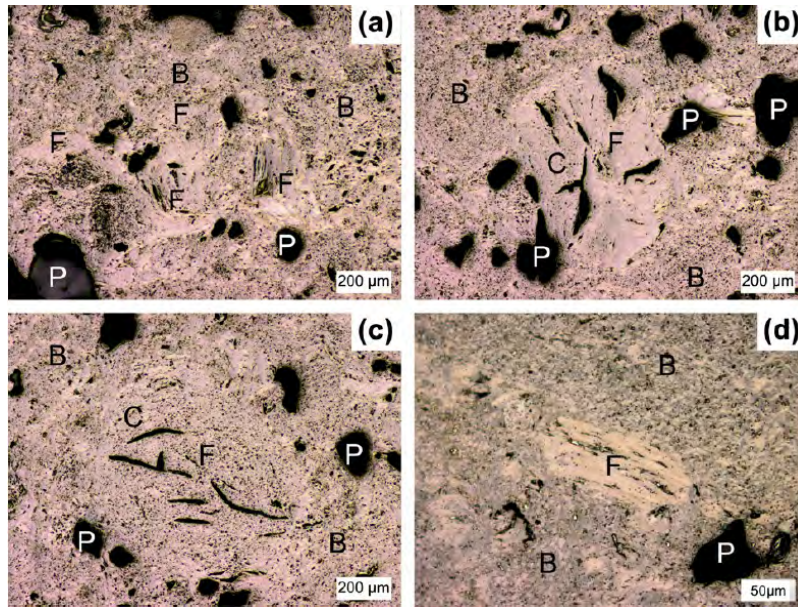
Fig. 5. Optical micrographs of PCEA graphite: (a) bright-field image showing filler particles with various shapes; (b) bright-field micrograph of filler with a relatively high degree of crystallite alignment surrounded by binder matrix; (c) bright-field micrograph of roughly spherical filler particle; and (d) bright-field image of relatively small acicular filler particle. P = Porosity, F = Filler, B = Binder, C = Shrinkage crack.

Pore structure analysis

The three different types of porosity within nuclear graphite are gas-evolved pores, shrinkage cracks, and micro-cracks [8,20]. Pore characterization via image analysis used in the present study was able to resolve only gas-evolved pores and shrinkage cracks. As observed in Figs. 2–5, the porosity varies greatly in size, shape, and orientation between and within grades. A statistical summary of the data collected is given in Table 2.

Table 2   Statistical summary of pore analysis. Mean = arithmetic mean; W. Mean = weighted mean based on each pore's fractional contribution to total porosity.

Grade	Area (μm^2)					Eccentricity		Additional	
	Mean	W. Mean	σ	Min	Max	Mean	σ	Porosity (%)	Count
PGX	197.9	21,400	2047	12.1	353,336	0.820	0.14	21.49	475,981
PCEA	146.8	30,100	2097	12.1	447,960	0.814	0.14	15.98	1,242,597
NBG-18	168.3	23,600	1986	12.1	505,123	0.816	0.14	13.97	916,076
IG-110	98	485	195	12.1	27,868	0.798	0.14	14.73	1,532,451

Table 2 is the culmination of multiple samples of each grade covering areas of approximately 10 cm² for IG-110, NBG-18, and PCEA and an area of roughly 5 cm² for PGX. Such areas provided both large pore counts (on the order of 106) and were sufficient to observe variation within a grade. The arithmetic mean indicates that the distribution in pore size is skewed greatly toward the minimum pore size compared to a normal distribution. Examination of the weighted mean suggests that the majority of the total porosity is a result of a minute quantity of large pores in PGX, PCEA, and NBG-18. In IG-110 the opposite appears to be true. The majority of the total porosity results from smaller pores as suggested by the weighted average. The mean eccentricity of the pores ranged from 0.798 for IG-110 to 0.82 for PGX, corresponding to aspect ratios of 1.66 and 1.75, respectively. A somewhat unexpected result was seen in the calculated porosities of the grades. NBG-18 was calculated to have an overall porosity of 14%, followed by IG-110 with 15%, PCEA with 16%, and PGX with 21%. This result was unexpected given that visual inspection of IG-110 did not reveal significant porosity, while porosity was very

apparent in NBG-18. The porosity was calculated by dividing the total pore-area by the total area observed. For this calculation to be valid, the porosity must be nearly uniform throughout the graphite block. Using the theoretical densities of each graphite grade, apparent densities were back-calculated and compared to their respective values from the manufacturer (Table 3).

Table 3   Summary of density values determined experimentally, reported by manufacturers, and calculated theoretically from lattice parameters.

Grade	Experimental (g/cm^3)	Manufacturer (g/cm^3)	Theoretical (g/cm^3)
PGX	1.772	–	–
PCEA	1.896	1.84	2.257
NBG-18	1.938	1.85	2.253
IG-110	1.925	1.77	2.257

The experimental apparent densities were all in excess of those listed by the manufacturer. For IG-110, NBG-18, and PCEA the errors, relative to the manufacturer's value, were 8.8%, 4.8%, and 3.1%, respectively. This positive error may occur as a result of an overestimation of pore area due to the choice of thresholding parameters. In a nuclear grade such as IG-110, size and proximity of the porosity can lead to connection of pores after thresholding. Such errors can be minimized, and experimentor bias can be removed to some degree, by the use of automated global thresholding methods [15,21]; however, from visual inspection of optical micrographs it is difficult to accept that manufacturer-reported porosity of IG-110 is very similar to that predicted for PGX. Another possibility is that the manufacturers' values were derived from fluid intrusion methods that were incapable of accessing all of the porous volume. This would result in an underestimation of the apparent densities. Regardless, this comparison is made to show the relative accuracy of measurements via digital image analysis.

Inspection of the resulting data for pore orientation showed an approximately normal distribution of orientation with respect to the horizontal image plane. To confirm the existence of a preferred orientation within the porosity, three mutually orthogonal samples were taken from each grade (IG-110, NBG-18, and PCEA). Resulting orientations were fitted to normal distributions and the standard deviation, σ, for each sample was tabulated. As seen in Table 4, NBG-18 and PCEA have only two statistically different standard deviations, implying a preferential orientation of porosity within the grades. IG-110 has three statistically significant means; however, two are relatively close to one another, which is assumed to be a result of imperfect slicing along the three orthogonal planes resulting in slight displacements of the standard deviations from their true values. While these results (Table 4) indicate the existence of preferential pore orientation, they do not provide significant evidence as to the magnitude or variation of the orientation upon processing of the original block. To obtain that data, detailed information about sampling location relative to the original block and the block's orientation relative to processing would need to be known. It should be noted that there was no significant change in the distribution of pore area or shape with sample position or orientation. The orientation distribution observed in each cross section does not appear to change as a function of pore area.

Table 4   Tabulated standard deviations from fits of normal distributions, with α = 0.05, to the pore-orientation distributions. A slight preferential orientation of the long axis of pore was observed. Sample population per face ranged from ~87,000 to ~327,000 pores.

Grade	Face 1	Face 2	Face 3
PCEA	52.37 ± 0.14	49.19 ± 0.16	48.87 ± 0.17
NBG-18	49.82 ± 0.23	49.74 ± 0.17	47.82 ± 0.15
IG-110	51.75 ± 0.13	50.68 ± 0.13	43.00 ± 0.11

Since proprietary details of processing are only approximately known for each grade, it is difficult to conclude the exact reasoning for the observed pore orientation; however, it is suspected that the orientation is the result of densification impregnations. Gas evolved from the impregnation material will take the path of least resistance corresponding to the path through the impregnated pores to the nearest surface. If all three orthogonal faces are equally far from the point of gas evolution, there will be no preferred alignment of the porosity. When the point of gas evolution has different path lengths to the graphite block surface, preferred alignment will result. Using this hypothesis, the degree of preferred orientation will be dependent upon the position of the examined sample with respect to the original graphite block.

While useful, the statistical data above do not fully describe the nature of the pores within each grade. The quantity of pores within any given size range was found to be a strong function of pore size. The shape of porosity, while not strongly dependent on pore size, had a wide distribution. In general, the aspect ratio of a pore ranged from 1 to 25. To better describe pore quantities and shape, continuous distributions were fitted to the experimental data collected. A plot of pore frequency/cm^2 vs. pore area ranging from 12 μm^2 to 2000 μm^2 is shown in Fig. 6. Although significantly larger pores were observed in each grade, more than 98% of the pore data fell within this range. The ~2% remaining was discarded to allow a 'better' fit of the remaining data. Initial inspection of plotted data displays the approximate "power-like" nature of pore frequency vs. size. Transformation of the dependent and independent variables by a natural logarithm yielded approximately linear functions (Fig. 6). The pore area, while expressed in units of μm^2, was really measured as a discrete function of pixel quantities.
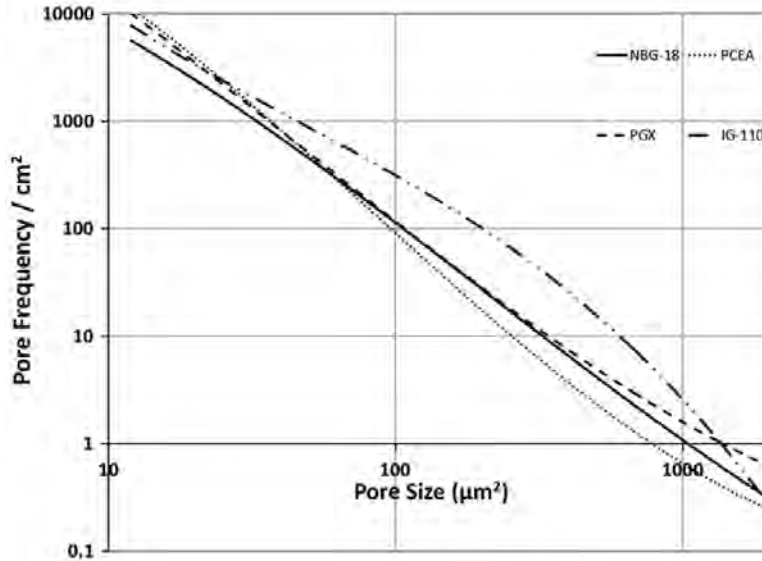
Fig. 6.   Log–log plot of frequency of pore size per cm^2 as a function of pore size.

The final distributions were deemed best fit by a third-order polynomial with the natural log of the pore area as the independent variable (Table 5).

$$ln(y(x)) = a + bln(x) + cln(x)^2 + dln(x)^3$$

Here, x is pore area in μm^2 and y is frequency per cm^2. Higher-order polynomials naturally provided higher R^2 values and lower root-mean-square errors; however, the rate of increase in 'fit improvement' dropped significantly with increasingly higher orders. The general logarithmic

nature of the pore area distribution in PCEA appears to coincide well with similar image analysis techniques used by Contescu for PCEA [16].

Table 5   Coefficients for fitting area distributions of each graphite grade.

Grade	a	b	c	d
PGX	13.416385	-1.220592	-0.240437	0.0211058
PCEA	12.045997	0.0249847	-0.552325	0.0416005
NBG-18	11.072113	-0.26909	-0.339038	0.0213758
IG-110	15.431958	-3.794709	0.6107167	-0.05282

The shape of the porosity as described by the eccentricity of an ellipse is shown in Fig. 7. By inspection, it is apparent that each grade has a relatively similar distribution, with the largest deviation occurring in the curve for IG-110. This deviation of IG-110 from the other grades is hypothesized to be the result of the green-body formation via isostatic press. Fig. 7 suggests that only a minority (~6%) of the total pores may be described as approximately spherical while nearly 75% of the pores examined have aspect ratios between 1.5 and 5. The average aspect ratio of porosity in nuclear graphite is approximately 1.7 and ranges from a low of 1.66 for IG-110 to a high of 1.75 for PGX.
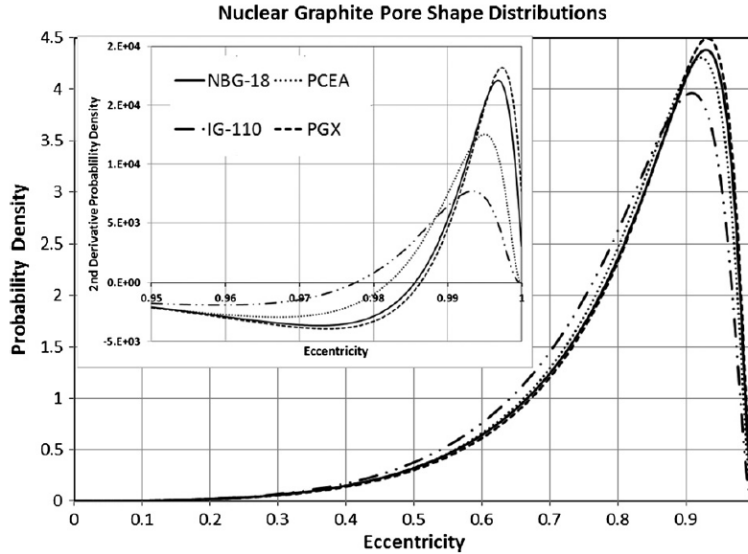

Fig. 7.   Continuous probability distribution functions of porosity shape described by eccentricity of an ellipse. Inset plot is the second derivative of the density function over the range of $0.95 \leq e \leq 1$.

The shape of the experimental-data curve for eccentricity was best fit by the Johnson S_B continuous distribution function. The Johnson S_B follows the general form

$$f(x) = \frac{\partial}{b(1-b)} \phi(z)$$

where $z = \gamma + \delta \ln (b/(1 - b))$, with $b = (x - \theta)/\sigma$, and ϕ is the standard normal distribution (Table 6). For this function, γ and δ are shape parameters while θ and σ define the location and shape of the curve, respectively. The peaks of each function are located at eccentricities of 0.908, 0.931, 0.929, and 0.922 (aspect ratios of 2.389, 2.747, 2.704, and 2.579) corresponding to IG-110, PGX, NBG-18, and PCEA, respectively. The probability of a pore existing with an eccentricity less than that of peak density is approximately 0.78 and ranges from 0.773 to 0.797.

Table 6   Parameters for Johnson S_B fit of pore eccentricity.

Grade	γ	δ	θ	σ
PGX	-1.930488	1.0427341	-0.059312	1.0607131
PCEA	-1.948658	1.0762906	-0.080897	1.0810973
NBG-18	-1.883605	1.0386604	-0.050993	1.051878
IG-110	-1.862962	1.1055111	-0.068859	1.0690328

Since two types of pores were observed, gas-evolved porosity and shrinkage cracks, with very different shapes, it was initially hypothesized that the pore shape distribution would be bimodal. As seen in Fig. 7, this hypothesis is invalid. The shape distribution of porosity in nuclear grade graphite shows no obvious transition between shrinkage cracks and gas-evolved porosity. To estimate the shrinkage crack contribution to total porosity the following assumption was made: the second inflection point in the continuous distributions is located at the eccentricity value where shrinkage cracks become the dominant observation. Using this criterion it was found that shrinkage cracks account for a fraction ≥ ~0.9% of IG-110 pores, ~0.6% of PGX pores, ~0.6% of NBG-18 pores, and ~0.8% of PCEA pores. This result appears to visually coincide with the optical micrographs of each grade. The average aspect ratio of the inflection point was approximately 5.5.

From the examination of pore shape as a function of pore area, it was observed that the shape distribution function is slightly dependent on pore area. As the pore size increases, the probability density near the peak position increases and becomes a maximum near ~100 μm^2 for NBG-18 and PCEA (Fig. 8). For IG-110 this peak occurs at approximately 300 μm^2. There is also a slight shift in the peak position to higher eccentricities that occurs in each grade. As the pore area is increased, this shift becomes much smaller. While there is a slight dependence of the shape distribution on pore area, the overall fit is exceptional over the entire range of pore area.
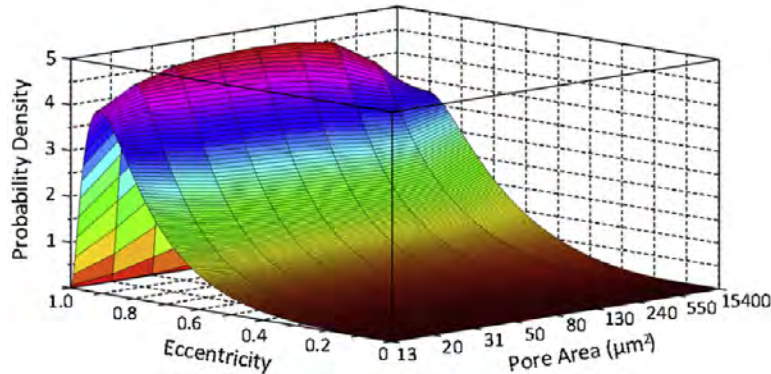

Fig. 8.   3D plot of the probability density of various pore shapes (eccentricity) for various ranges of pore area; the pore area given is the log-mean average of the range of pore areas used.

References

1. R. Bratton, W. Windes, NGNP graphite selection and acquisition strategy, ORNL/TM-2007/153-10-07 (INL/MIS-10-19427), Oak Ridge National Laboratory, July 28, 2010.
2. W. Windes, T. Burchell, R. Bratton, Graphite technology development plan, INL/EXT-07-13165, Idaho National Laboratory, September 2007.
3. T.D. Burchell, Carbon 34 (1996) 297–316.
4. R.E. Nightingale, Structure, in: R.E. Nightingale (Ed.), Nuclear Graphite, Academic Press, 1962, pp. 87–115.
5. K. Wen, J. Marrow, B. Marsden, J. Nucl. Mater. 381 (2008) 199–203.
6. N. Otsu, IEEE Syst. Man Cybern. 9 (1979) 62–66.
7. C.I. Contescu, T.D. Burchell, Characterization of porosity development in oxidized graphite using automated image analysis techniques, ORNL/TM-2009/192, 2009.

Microstructural Characterization of Next Generation Nuclear Graphites

Summary
The microstructural characteristics of various petroleum- and pitch-based nuclear graphites (IG-110, NBG-18, and PCEA), which are of interest to the next-generation nuclear--plant program, have been studied via transmission electron microscopy. Bright-field imaging was used to identify and understand the different features constituting the microstructure, including filler particles, microcracks, binder phase, rosette-shaped quinoline insoluble (QI) particles, chaotic structures, and turbostratic graphite. The dimensions of microcracks were found to vary from a few nanometers to tens of microns; furthermore, the microcracks were found to be filled with amorphous carbon of unknown origin. The pitch-coke-based graphite (NBG-18) was found to contain a higher concentration of binder phase containing QI particles as well as chaotic structures. The turbostratic graphite, present in all of the grades, was identified through its elliptical diffraction patterns. The differences in the microstructure have been analyzed in view of the different processing conditions involve for each grade.

Experimental details
Transmission electron microscopy (TEM) specimens of these graphites were prepared via conventional sample-preparation techniques. Bulk samples of NBG-18 (SGL Group, Wiesbaden, Germany), PCEA (GrafTech International, Parma, OH, USA), and IG-110 (Toyo Tanso Co., Kagawa, Japan) were obtained from the manufacturers. Disks with 3 mm diameters were cut from the as-received bulk graphite using a diamond saw. These disks were further thinned mechanically to approximately 20–30 mm. A precision ion polishing system (Gatan PIPS 691, Gatan, Inc., Pleasanton, CA, USA) was used to achieve the final electron-transparency. Ion-milling conditions were optimized to minimize the ion-beam damage. Typically, the samples were milled for about 60–70 min at 5° followed by a low-angle milling step at 2° for 10 min. TEM studies were performed at room temperature on a 200 kV high-resolution instrument (JEOL-2100, JEOL Ltd., Tokyo, Japan).

Results
Figure 2 shows the various microstructural features of the IG-110, which is a fine-grained isotropic graphite fabricated via cold isostatic pressing. Petroleum coke is used as the filler material. Figure 2a shows what appears to be a filler particle (marked F) surrounded by binder (marked B) on both sides. The filler particles are lenticular in shape with sizes varying from a few tens of nanometer to tens of micrometers in length. The width varies from a few tens of nanometers to hundreds of nanometers. The lenticular shape arises from the shape of the starting coke particles. When the highly crystalline coke particles are crushed, they cleave parallel to basal planes resulting in a powder containing elongated particles with their crystallographic *c*-axes perpendicular to the length of the particles [1]; thus, the shape of the resultant filler particles depends on the crystallinity of the coke used. Petroleum coke is usually highly crystalline, whereas pitch coke is usually less crystalline, resulting in more spherical filler particles. It should also be noted that the quality of the coke can vary depending on the crude oil/coal-tar pitch source used, affecting the shape distribution of the resultant filler particles significantly. Figures 2b and 2c are at a higher magnification and show the filler particles in different regions. The filler particles (as well as the binder) contain cracks running parallel to the basal planes. Microcracks are believed to form through delamination of the basal planes as a result of thermal contraction, and they play a major role in the irradiation-induced swelling process as well as the thermal-expansion characteristics of the graphite. It was originally thought that these cracks would be void of any material, but most are filled with amorphous carbon, the origin of which is not clear. This observation is in accordance with the recent study by Wen *et al.* [2] who, despite preparing samples using several methods, noticed the presence

of amorphous carbon in the microcracks of PGA grade nuclear graphite. The present authors show that this is a characteristic of *all* nuclear graphites irrespective of the manufacturing process.
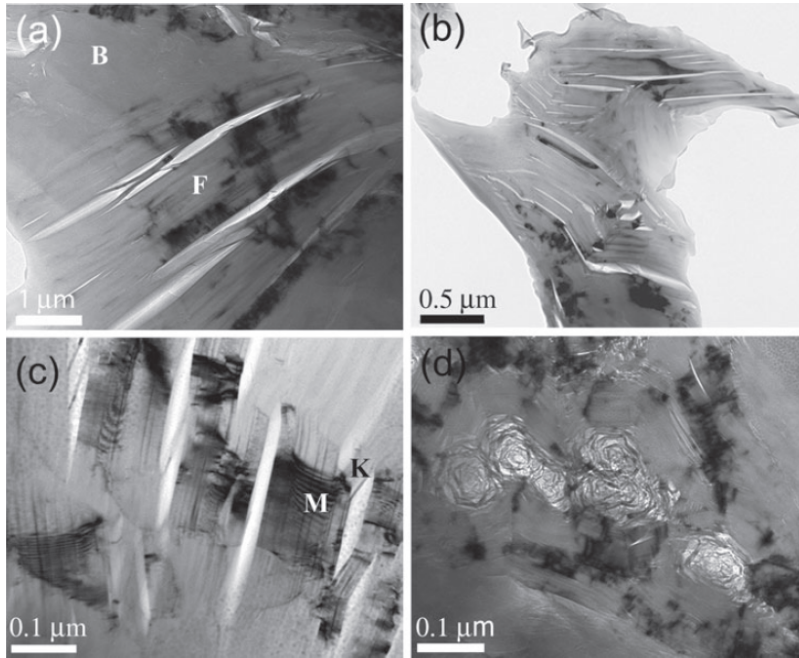

Fig. 2　Bright-field TEM micrographs of IG-110 grade graphite: (a) interface region between a filler particle (marked F) and binder (marked B); (b) filler particle at high magnification; (c) filler particle with kink boundaries (marked K) and Moiré fringes (marked M); and (d) binder region

Figure 2c shows the presence of delamination cracks with strands of inclined basal planes (marked K) bridging the bulk of the crystal across the cracks. These inclined strands, commonly known as kink bands, arise as a localized deformation mechanism in a variety of materials. Materials with layered structures such as graphite, boron nitrides, *etc.*, subjected to compressive stresses are especially prone to this kind of localized deformation [3]. Another interesting feature of Figure 2c is the appearance of Moiré fringes (marked M), which indicates the presence of twist boundaries, confirmed by the selected-area electron-diffraction pattern (SADP) shown in Figure 3a. The [010] pattern clearly shows the arcing of the spots, indicating the presence of low-angle twist boundaries that may be a result of the delamination process.
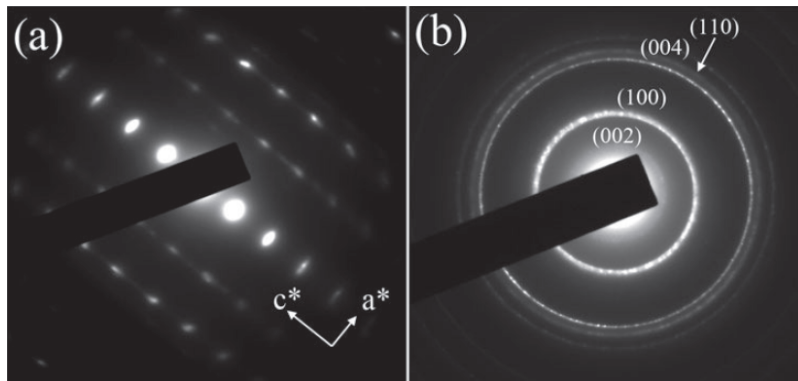

Fig. 3　SADPs recorded from (a) filler particle and (b) rosette in the binder region of IG-110 graphite

26

Figure 2d shows a micrograph recorded from the binder region. The binder region was found to contain well-graphitized crystallites of carbon with occasional rosette-structured particles embedded in them. Binder regions were also found to contain cracks similar to that of the filler particles. The rosette-shaped particles are well crystallized and are thought to originate from the QI fraction present in the pitch [1]. Even though it is very difficult to quantify the concentration of these particles using TEM due to the limited field of view and heterogeneity of the microstructure, the authors estimated about 10–20 particles per square micron in the binder region. The size of these rosettes varied from 10 nm to a few hundreds of nanometers in diameter. The SADP recorded from a rosette is shown in Figure 3b with the prominent rings indexed as 002, 100, 004, and 110. The ring pattern is a result of the continuous spiraling of the graphitic strands, which is equivalent to texturing in a direction perpendicular to the *c*-axis.

QI particles are basically solid particles similar to carbon black, composed of high-molecular-weight hydrocarbons [4, 5]. These particles are formed either during the decomposition of coal or through the condensation of small aromatic molecules on the walls of the cracking chamber. It is believed that the aromatic molecules result in rosette-shaped particles constituting a spiral of graphite strands during graphitization. These strands are more disordered at the center of the rosettes. It can also be seen that these rosettes act as templates inducing the graphitization of binder around them in the form of wide concentric strands of graphite (marked with a dotted arrow in Fig. 2d) retaining the crystallographic orientation of the outermost strand of the rosette. The concentration of QI particles in coal tars can vary from 2 to 12 wt% depending on the type of coal used and the production conditions. Unfortunately, the exact concentrations are proprietary and so not revealed by the manufacturers.

The presence of QI particles has been known to affect the mechanical properties of graphite [6]. Studies have shown the compressive strength of graphite to vary significantly with QI-particle concentration, and there appears to be an optimum concentration where compressive strength is maximized. During baking, QI particles provide paths facilitating the escape of volatile species that reduce cracking and hence increase the strength of the final product [6].

Figure 4 shows the microstructural features of NBG-18 grade graphite. NBG-18 is a vibrationally molded, near-isotropic graphite with pitch coke as the filler source. Figure 4a shows an interface region between a filler particle (marked F), binder phase (marked B), and turbostratic graphite (marked T). Figure 4b shows the close-up view of a filler particle delaminated into several fine stands (~10 nm in width) of graphite resulting in numerous microcracks. Several filler particles with such fine strands were observed while other particles exhibited only a few cracks, similar to IG-110. One of the striking features of the NBG-18 microstructure is the high concentration of binder and QI particles (Fig. 4c) compared to other grades under study. The authors observed the presence of 40–60 QI particles of varying sizes in a given square micron of binder. One of the reasons for the high concentration of the QI particles could be the usage of coal-tar pitch (as the binder source), which naturally tends to have a high concentration of QI particles [1]. Figure 4d is a high-magnification image depicting the internal structure of a QI particle, and the diffraction pattern obtained was similar to that in Figure 3b. The interior of QI particles appears to be more chaotic in the case of NBG-18 compared to other grades.

Apart from the QI particles, the binder phase in NBG-18 showed the presence of several other types of spherical chaotic structures as shown in Figure 5. These structures are ~1 μm in diameter and packed with randomly oriented well-crystallized graphitic strands. Similar structures have been observed in PGA grade graphite [7], which has a coal-tar pitch binder; therefore, it can be safely concluded that these structures are characteristic of coal-tar pitch

based binders. The diffraction patterns recorded from these chaotic structures were similar to those of QI particles.
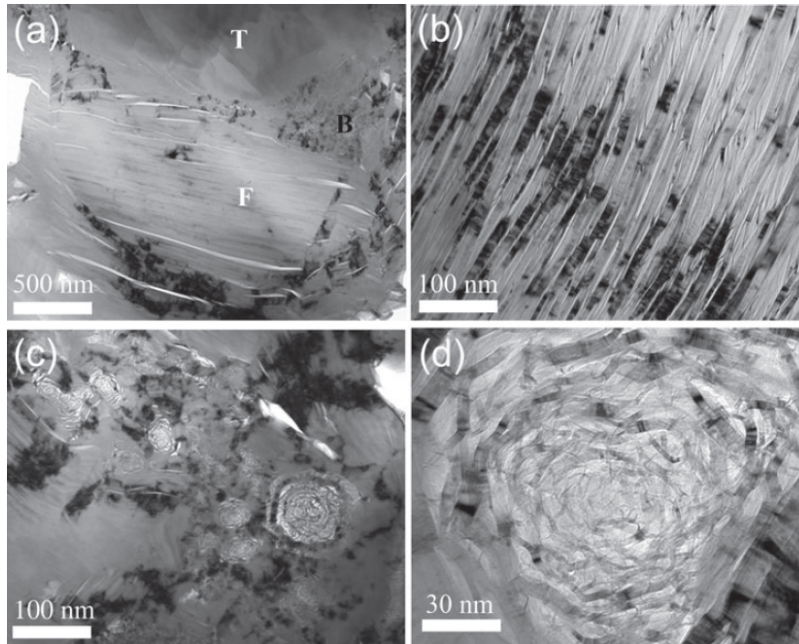

Fig. 4   Bright-field TEM micrographs of NBG-18 grade graphite: (a) interface region constituting filler (marked F), binder (marked B), and turbostratic graphite (marked T); (b) filler particle at higher magnification, (c) binder region, and (d) rosette (QI particle) at high magnification
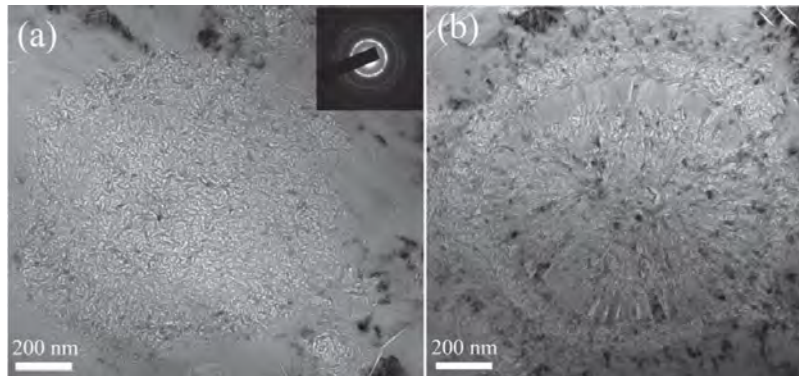

Fig. 5   Bright-field TEM micrographs of spherical chaotic structures in NBG-18 grade graphite and typical SADP (inset) recorded from these structures

The microstructural features of PCEA graphite, which is a nearly-isotropic, extruded, petroleum coke based graphite, are depicted in Figure 6. Figure 6a shows an interface region between a filler particle (marked F) and binder phase (marked B) with embedded QI particles. Figure 6b shows the structure of a filler particle with microcracks. The microcracks in the case of PCEA appear to be wider than in other grades.   Another distinct feature of PCEA is that the amorphous carbon filling the microcracks contains numerous voids. The sizes of these voids were found to vary in the range of approximately 1–25 μm in diameter. Figures 6c and 6d show the microstructure of the binder phase and a QI particle, respectively. The concentration of QI particles is comparable to that in IG-110. It should be noted that, unlike NBG-18, petroleum based pitch is used in the production of both IG-110 and PCEA, so they are expected to have negligible amounts of QI particles.
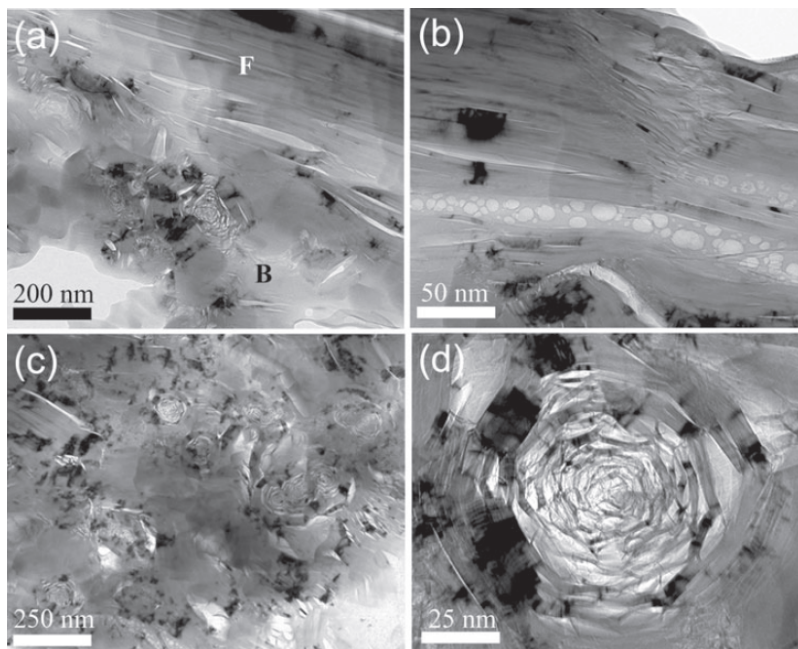
Fig. 6 Bright-field TEM micrographs of PCEA grade graphite: (a) interface region constituting filler (marked F) and binder phase (marked B); (b) filler particle with cracks filled with porous amorphous carbon; (c) binder region; and (d) a rosette at high magnification

Apart from the above-mentioned structures that constitute well-crystallized graphite, the authors also noticed the presence of turbostratic graphite in all the graphite grades. Figure 7 shows a typical microstructure of turbostratic graphite and the corresponding SADP recorded from IG-110. Turbostratic graphites can be identified via electron diffraction by their elliptical diffraction patterns. Turbostratic graphite has close-packed carbon planes that are curled and rotated with respect to each other. The atoms are arranged in layers similar to those in graphite, but they are stacked randomly. The presence of simultaneous translational and rotational disorder results in the distribution of the scattering power in the reciprocal lattice in the form of concentric cylinders. The sectioning of these cylinders by the Ewalds sphere gives rise to a series of elongated spots that lie on one ellipse [8]. As pointed out by Vainshtein *et al.* [9], one could index the spots on one ellipse with the same *hk* but different *l* indices, as shown in Figure 7b. Turbostratic graphite can form during the process of graphitization or normal graphite can be converted into the turbostratic form by weakening of the bonding between the layers by, for example, mechanochemical activation [10]. There is also a possibility of the accidental insertion of Ar^+ ions between the layers during ion-milling, resulting in turbostratic graphite. To discount this effect, TEM studies were carried out on powdered samples of graphite by dispersing the flakes of graphite on a TEM grid without ion milling. TEM studies (Fig. 8) showed the turbostratic graphite to be present even in the case of the powder samples, confirming that the turbostratic graphite is an inherent constituent of the nuclear-graphite microstructure and not an artifact created by ion-milling.

There have been several attempts in recent times to model the irradiation-induced property changes in graphite, especially Young's modulus and dimensional changes, and to identify the probable microstructural mechanisms [11, 12]. These studies show that the changes in the physical properties under irradiation are highly dependent on the filler particle size as well as the porosity; however, the experimental results obtained from various test reactors have shown these changes to be highly complex, providing very little insight into the microstructural

mechanisms [13]. One of the reasons for the difficulty is the poor understanding of the role microstructure plays in defining the properties, and the authors hope that this project adds valuable information on that front.
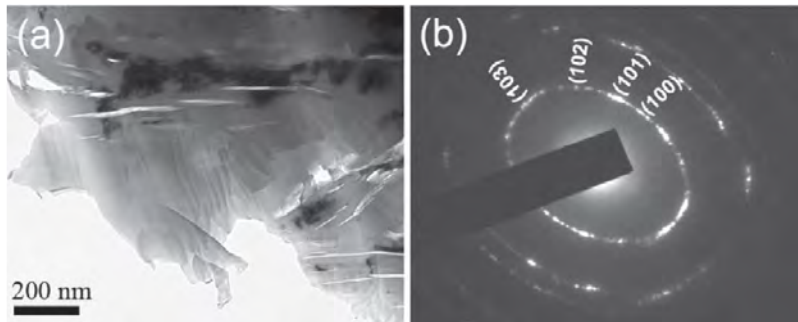

Fig. 7   (a) Bright-field TEM micrograph of turbostratic graphite recorded from IG-110 grade graphite and (b) the corresponding SADP
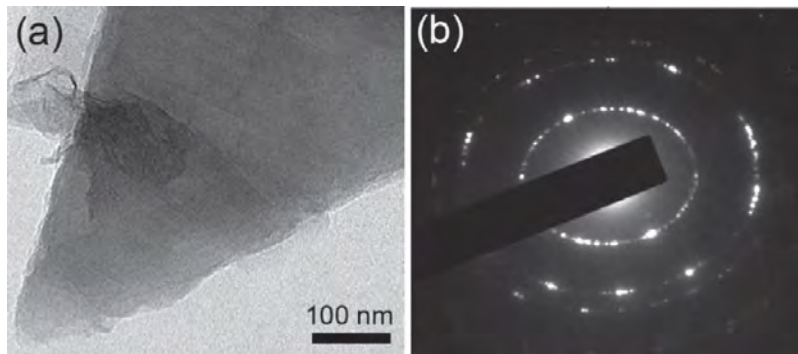

Fig. 8 (a) Bright-field TEM micrograph and (b) SADP recorded from powdered sample of IG-110 showing the presence of turbostratic carbon

References

1. Nightingale, R.E. (1962). *Nuclear Graphite*. New York: Academic Press.
2. Wen, K.Y., Marrow, J. & Marsden, B. (2008). Microcracks in nuclear graphite and highly oriented pyrolytic graphite (HOPG). *J Nucl Mater* **381**, 199–203.
3. Barsoum, M.W., Murugaiah, A., Kalidindi, S.R., Zhen, T. & Gogotsi, Y. (2004). Kink bands, nonlinear elasticity and nanoindentations in graphite. *Carbon* **42**, 1435–1445.
4. Mochida, I., Maeda, K. & Takeshita, K. (1978). Comparative study of the chemical structure of the disk-like components in the quinoline insolubles. *Carbon* **16**, 459–467.
5. Peaden, P.A., Lee, M.L., Hirata, Y. & Novotny, M. (1980). High-performance liquid chromatographic separation of high-molecular-weight polycyclic aromatic compounds in carbon black. *Anal Chem* **52**, 2268–2271.
6. Morgan, M.S., Schlag, W.H. & Wilt, M.H. (1960). Surface properties of the quinoline-insoluble fraction of coal-tar pitch. *J Chem Eng Data* **5**, 81–84.
7. Wen, K.Y.,Marrow, T.J. &Marsden, B.J. (2008). The microstructure of nuclear graphite binders. *Carbon* **46**, 62–71.
8. Schiffmacher, G., Dexpert, H., Caro, P. & Cowley, J.M. (1980). Elliptic electron diffraction pattersn from the films of turbostratic graphite. *J Microsc Spectrosc Electron* **5**, 729–734.
9. Vainshtein, B.K., Zuyagin, B.B. & Avilov, A.V. (1992). Electron diffraction structure analysis. In *Electron Diffraction Techniques I*, Cowley, J.M. (Eds.). New York: Oxford University Press.
10. Salver-Disma, F., Tarascon, J.M., Clinard, C. & Rouzaud, J.N. (1999). Transmission electron microscopy studies on carbon materials prepared by mechanical milling. *Carbon* **37**, 1941–1959.
11. Hall, G., Marsden, B.J. & Fok, S.L. (2006). The microstructural modelling of nuclear grade graphite. *J Nucl Mater* **353**, 12–18.
12. Bradford,M.R. & Steer, A.G. (2008). A structurally-based model of irradiated graphite properties. *J Nucl Mater* **381**, 137–144.
13. Simmons, J.W.H. (1965). *Irradiation Damage in Graphite*. New York: Pergamon Press.

Oxygen transfer model for high purity graphite oxidation

Summary
An intrinsic mathematical model is developed for the investigation of the gas–solid reaction kinetics of high-purity graphite and oxygen. This model is based upon the oxygen transfer mechanism and uses physically meaningful parameters that are directly comparable to the experimental and theoretical literature of the carbon–oxygen reaction system. The model was used to extract reaction parameters for NBG-18 polycrystalline graphite for oxygen/nitrogen mixtures with a total pressure of 100 kPa. Experimental temperatures ranged from 500 to 850°C for oxygen partial pressures of 1, 5, 10, 20, and 40 kPa. The optimized model parameters are in good agreement with previously reported literature values.

Experimental details
Porosity in a carbon material greatly complicates the oxidation kinetics of the bulk material. Near 700 °C (Fig. 1), the oxidation of the bulk graphite in this study is well within the regime of pore diffusion [30]. While the temperature range of the kinetic regime can theoretically be expanded by a substantial increase in the gas velocity over the graphite surface, filler-particle fall out and changing surface area throughout the reaction are difficult to account for directly.
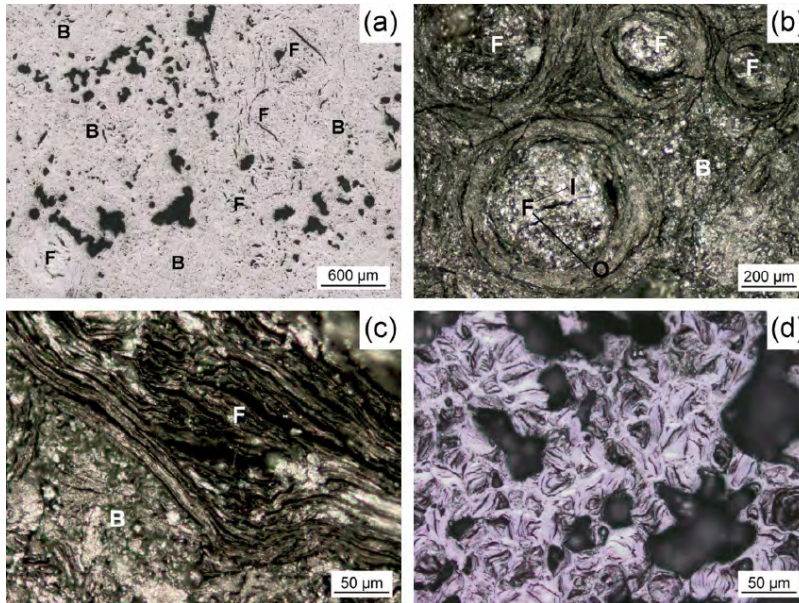

Fig. 1   *Various features of NBG-18 polycrystalline graphite are shown, including the filler, F, both inner, I, and outer, O, layers as well as the binder, B; (a) the virgin NBG-18 microstructure; (b–d) oxidized NBG-18 filler; (b) the inner and outer layers of the typically spherical filler particles; (c) the high degree of alignment of crystallites in the outer layers of the filler particles relative to the binder; (d) the random orientation of crystallites in the filler particle interiors. For (b and c) samples were oxidized for 30 min at 700 °C. For (d) graphite was oxidized using $K_2Cr_2O_7$ in concentrated sulfuric acid [8].*

Graphite Powder
To avoid the convoluting effects of porosity on the reaction kinetics and develop an intrinsic reaction model, graphite powder was used. NBG-18 graphite powder was prepared from bulk NBG-18 using a percussion mortar and pestle. A particle density of 2.23 g/cm^3 (99% theoretical density) was measured using a helium pycnometer (Quantachrome, USA) upon passage through a 500 mesh (25 µm) sieve. The particle size distribution was measured using a laser diffraction particle size analyzer (Partica LA-950, Horiba, Japan) via a wet method in distilled

water. The particle size was normally distributed with a mean of 12.9 µm and a standard deviation of 4.6 µm, confirmed by inspection using an analytical scanning electron microscope (SEM) (Hitachi S-3400N-II, Hitachi, Japan).

The reactivity of carbon is known to vary with the level of impurities [30,32,67,68]. The NBG-18 graphite used in this study did not undergo the additional purifications required for nuclear applications [4]. The results of elemental analysis via inductively coupled plasma mass spectrometry (ICP-MS) are shown in Table 1. Impurity levels were assumed negligible in terms of their participation in the overall observed rate of oxidation.

Table 1   The 12 main impurities in NBG-18 from elemental analysis via ICP-MS.
Quantities are given in terms of mass fraction.

Element	ppm	Element	ppm	Element	ppm
Si	38	Fe	4.8	Hg	<0.5
Ca	5.9	F	<1	Mg	<0.5
Ta	<5	B	0.57	Pb	<0.5
S	4.8	Cr	<0.5	Sb	<0.5

Powder oxidation experimental setup
The overall rate of carbon consumption

$$a\mathrm{C}_{(s)} + \mathrm{O}_{2(g)} \rightarrow \mathrm{products}_{(g)}$$
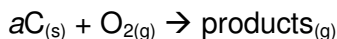
for NBG-18 was measured via thermogravimetric analysis (STA 449 F3 Jupiter, Netzsch, Germany). Experiments were performed isothermally between 500 and 850 °C. The absolute pressure within the reaction chamber was constant at approximately 100 kPa. The gas flow rate was maintained at 270 standard cubic centimeters per minute (sccm) to decrease the likelihood of mass transfer playing a significant role in the observed kinetics. The inlet gas was composed of 7.4 mol% argon, a protective gas for the balance chamber of the analyzer, and varying amounts of oxygen and nitrogen. Five oxygen partial pressures were investigated: 1, 5, 10, 20, and 40 kPa.

All experiments were conducted with 15 ± 0.5 mg of well-mixed NBG-18 powder placed in an alumina crucible (6mm diameter, 4 mm high). Alumina was shown by Ranish et al. [69] to be an inert material in the carbon–oxygen reaction system. Prior to running an experiment, the graphite samples underwent a vacuum and purge cycle to remove adsorbed moisture. Immediately thereafter samples were ramped to the reaction temperature at a rate of 20 °C/min in nitrogen at 50 sccm. Upon reaching the reaction temperature, the system was allowed to stabilize thermally for 30 min in nitrogen. The nitrogen flow was increased in two 100 sccm steps to 250 sccm over the first 5 min of the thermal stabilization dwell. After the allotted 30 min, the gas mixture was switched to the desired oxygen/nitrogen mixture with a total flow rate of 250 sccm. Each set of experiments was duplicated at least once for greater statistical certainty. A correction file was run at each temperature and partial pressure to account for errors in gravimetric measurements due to changing gas flows and thermal drift over longer experiments (>36 h). Residual powder was collected for post-examination. The excess oxygen ratio, EOR, was used as a figure of merit to help ensure that transport effects did not interfere with kinetics measurements. The EOR was calculated as the difference between oxygen molar flow rate and rate of carbon consumption, relative to the rate of carbon consumption, assuming the reaction product was entirely CO_2. Once the EOR fell below 10 for any significant portion of the experiment, higher temperature experiments were assumed null.

All gases were obtained from Praxair Inc. (CT, USA). The argon and nitrogen gases used were ultra-high purity grade. Oxygen was introduced via one of two primary standards containing 5% and 40% oxygen (by volume), respectively, and the balance nitrogen. Analytical uncertainty for the standard was guaranteed to be within ±2% of the reported oxygen concentration.

Electron microscopy
NBG-18 powder was examined pre- and post-oxidation using the SEM. Samples for TEM were analyzed to confirm assumptions made in the derivation of the shrinking-core model. The analysis confirmed preferential oxidation orthogonal to the basal plane and the absence of significant amounts of product film/ash on the graphite surface. TEM samples of NBG-18 (bulk material purchased from SGL group, Germany) were prepared by cutting thin bars, approximately 3 mm in length, from the as-received graphite. These bars were further thinned mechanically to a thickness of approximately 100 µm. An ion slicer (EM09100-IS, JEOL, Japan) was used to achieve the final electron transparency. Compared to conventional ion-milling techniques, the ion slicer produces minimal beam damage to the TEM samples. After initial examination in the TEM, samples were oxidized for 5 min with an oxygen partial pressure of 20 kPa at 600, 700, or 800 °C and re-examined. Examination took place at room temperature using a high resolution transmission electron microscope (2100-HR, JEOL, Japan) operated at 200 kV.

Arrhenius parameter estimation
The Arrhenius parameters for the oxygen transfer model were determined using an unconstrained nonlinear optimization implemented in MATLAB® (Matlab R2011a, Mathworks, USA). The optimization used a Nelder–Mead simplex direct search algorithm [70]. The minimization function was chosen specifically to mitigate substantial numerical error due to the large magnitudes and variation in parameter values with temperature and oxygen concentration. An initial guess vector for the optimization was chosen using a combination of available literature values, estimates from linear sections of the experimental Arrhenius plot, and visual inspection.

Results

Shrinking cylindrical platelet model
Derivation of the phenomenological shrinking cylindrical platelet model (SCPM) follows the approach of Levenspiel for a shrinking core [71,72]. In order to make inferences regarding the surface chemical reaction, the oxygen concentration at the surface must be known. If the reaction resistance is much greater than the gaseous mass transfer resistance, $1/k''_{eff} \gg 1/k_g$, and there is no/negligible ash or reaction product on the solid surface (a reasonable assumption for high-purity graphite), the concentration at the carbon surface is essentially that of the bulk gas stream.

In addition, for a traditional shrinking cylindrical core it is assumed that the chemical reaction did not occur on the top or bottom of the graphite platelets (graphitic basal planes) but only along the plate edges ((100) and (110) planes, Fig. 3a–c). In other words, it is assumed that the RSA is proportional to the plate edge area, $2\pi r l$. A TEM micrograph of an oxidized, quinoline-insoluble particle is shown in Fig. 3d. These particles, as depicted in the inset, are structured with the basal plane orthogonal to the particle's radial direction. The preservation of much of the particle along [*uv*0] visually suggests oxidation parallel to the (001) planes, as previously observed [46].
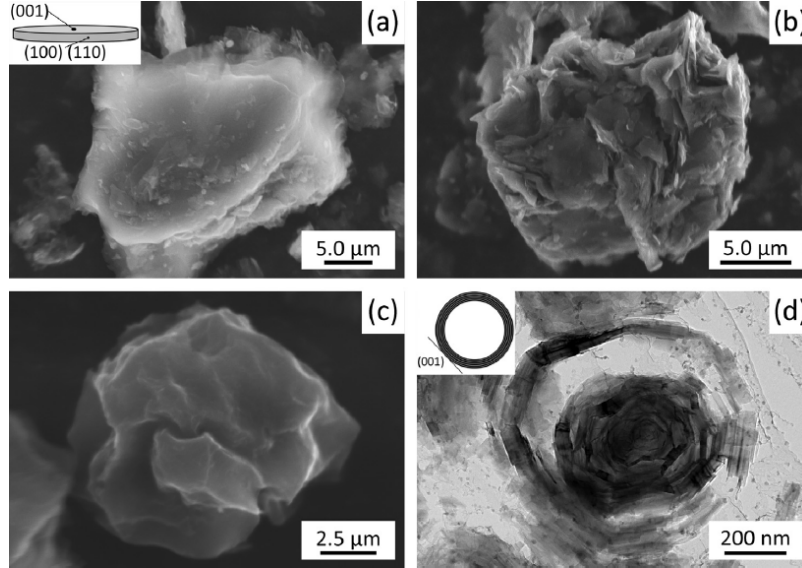
Fig. 3 Scanning electron micrographs of powder showing (a) a graphite platelet oriented as depicted in the inset, (b) a graphite platelet oriented on-edge, (c) a platelet oxidized at 575 °C to α 0.5 at PO_2 = 20 kPa, and (d) a transmission electron micrograph of oxidized NBG-18 binder showing a quinoline-insoluble particle oxidized at 700 °C for 5 min at PO_2 = 20 kPa.

The molar flux of carbon from the RSA of the graphite may be expressed as: $-N_c = ak''_{eff} \ |O_2|^n$; however, $N_c = (1/S_{ext})dn_c/dt$. The double prime above the reaction rate constant is used to denote that it is normalized with respect to the platelet edge geometric surface area, which is assumed proportional to the RSA. Upon integration the moles of graphite can be related to the cylindrical radius of the platelet through the molar volume:

$$1 - \frac{r}{r_0} = \frac{ak''_{eff} \ |O_2|^n}{r_0 \rho}$$

Typically, the term r/r_0 is replaced by an expression for the conversion of material to product defined here as α. For cylindrical platelet geometry the conversion is related to r/r_0 as $r/r_0 = (1 - \alpha)^{1/2}$. A plot of $1 - (1 - \alpha)^{1/2}$ vs. time will yield a straight line if the SCPM describes the physical progression of the reaction. The slope of such a plot contains information regarding the effective reaction order and the effective reaction rate constant. Both the reaction order and rate constant are generally expressed as effective parameters since gas–solid reactions typically involve many elementary steps within the overall reaction.

Throughout the entire experimental range, the SCPM was found to provide a reasonable fit of the experimental mass-loss data for all oxygen partial pressures. As observed in Fig. 4, the trend is highly linear, having a correlation coefficient greater than 99% for all experimental oxygen partial pressures. The slope of each curve was determined for $0.15 \leq \alpha \leq 0.85$. The deviation for $\alpha \leq 0.15$ may be explained by examination of electron micrographs in Fig. 3a and b. While the particle is approximated as a cylinder, it initially has a greater amount of ASA than the SCPM assumes. The surface area does smooth considerably upon further oxidation as shown in Fig. 3c. Deviation from the SCPM for $\alpha \geq 0.85$ can be explained by the observation that the platelets are made up of multiple crystallites. As α increases and platelet edge surface area decreases, the oxidation of the crystallite grain boundaries begins to contribute appreciably to the rate of oxidation, causing the experimental data to deviate slightly from the SCPM.

Additionally, the particle size distribution may have contributed to the deviation from the linear trend. The reaction rate observed was found to be insensitive to the level of conversion in the fitted range suggesting a pseudo-steady-state on the surface.
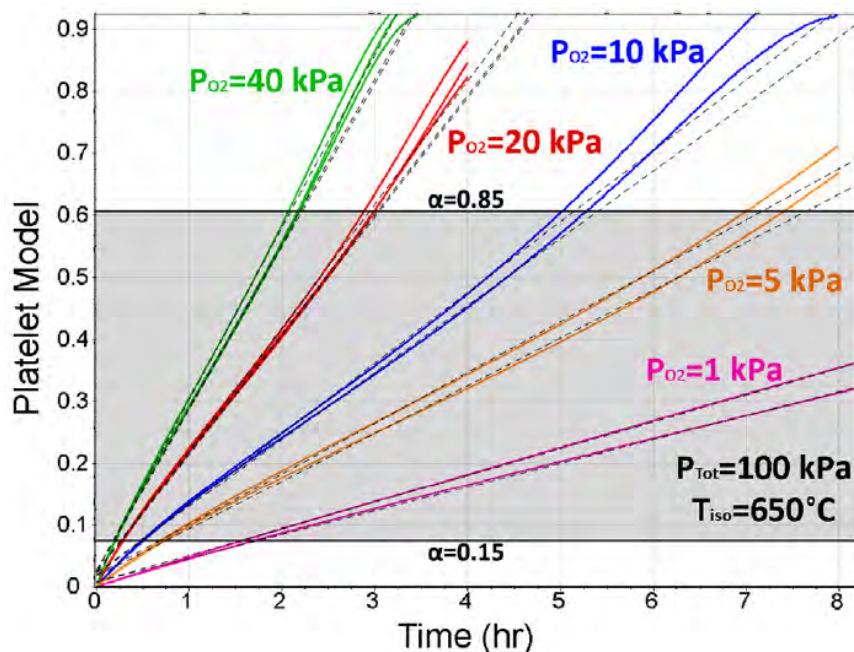

Fig. 4 The experimental measurements at 650 °C for 1, 5, 10, 20, and 40 kPa O_2 in N_2 of 1- $(1 - \alpha)^{1/2}$ vs. time. The error from individual data points and linear fits are insignificant relative to the error between measurements.

The SCPM did not provide an accurate description of the reaction above 725 °C for the higher oxygen partial pressures examined (10, 20 and 40 kPa). It was determined that gaseous transport effects became rate-limiting within the reaction system. As demonstrated in Fig. 5, the sample temperature rose 5 °C within a minute of oxygen introduction to the system. The irregular shape of the temperature peak and the negative temperature deviation of the curve are the results of the sample temperature controller set to maintain the isothermal set point. The sample thermocouple, as in many thermogravimetric setups, was located below the sample crucible, thus it is plausible that the sample temperature deviation was substantially greater than 5 °C; however, even a 5 °C change may be considered substantial given that the overall reaction rate was observed to approximately double with a temperature increase of 25 °C. The excess oxygen ratio also decreased significantly from initial values greater than 100 to approximately 3 and remained between 3 and 4 for a majority of the reaction. The low excess oxygen ratio brings into question the validity of the assumption that the surface oxygen concentration was equal to that of the bulk gas at high temperatures. Several methods are available for examining a system for which mass transfer and the chemical reaction must be considered [15,72–76]. These models rely on the use of mass-transfer correlations and introduce a much larger degree of uncertainty than desired in the current study; therefore, great care was taken to ensure that the mass transfer resistance was negligible.

Effective kinetics parameters
Since the graphite–oxygen reaction system is quite complex, the reaction order was initially assumed to be 1 with respect to oxygen. The resulting reaction rate constants are plotted in an Arrhenius plot for the oxygen isobars in Fig. 6a. The most notable feature is the lack of linearity

throughout the entire experimental temperature range. For 500–550 ℃, the apparent activation energy is approximately 160 kJ/mol. Between 600 and 725 ℃ this value increases to nearly 225 kJ/mol. These values agree quite well with typical overall activation energies of approximately 170–210 kJ/mol for carbon materials, including high-purity graphites [17–25,77]. Finally, above 750 ℃, the apparent activation energy decreases to roughly 30 kJ/mol. Two additional features observed are an increase in ak''_{eff} with decreasing oxygen partial pressure and the decrease in distance between the values of ak''_{eff} for a given set of oxygen partial pressures as temperature increases (Fig. 6a and b).
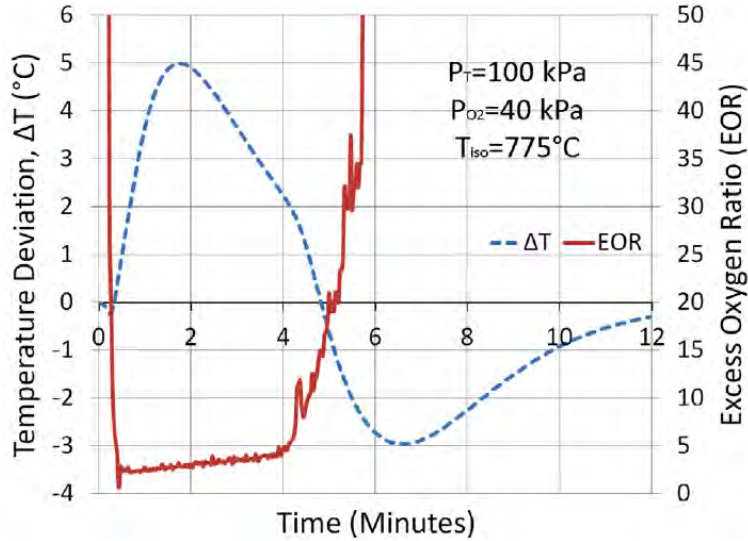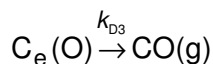

Fig. 5   The temperature deviation from the isothermal set point and EOR vs. time. A sample-temperature controller was used to minimize sample-temperature deviation.

Oxygen transfer model
The oxygen transfer mechanism (OTM) proposed by Radovic *et al.* [34–36] is thought to be a concise mechanism that is both sufficient and necessary to account for a majority of the known facts and experimental observations regarding the carbon–oxygen reaction system. Making a number of simplifying assumptions, an intrinsic rate equation can be written explicitly in terms of the reaction temperature and the concentration of molecular oxygen.

The OTM is comprised of the following reactions of the oxygen transfer mechanism:

$$C_e + O_2(g) \xrightarrow{k_{A1}} C_e(O_2)$$

$$2C_e + O_2(g) \xrightarrow{k_{A2}} 2C_e(O)$$

$$C_e(O_2) + C_b \xrightarrow{k_S} C_b(O) + C_e(O)$$

$$C_e(O_2) + C_b(O) \xrightarrow{k_{D1}} CO_2(g) + C_e(O)$$

$$C_e(O) + C_b(O) \xrightarrow{k_{D2}} CO_2(g)$$

$$C_e(O) \xrightarrow{k_{D3}} CO(g)$$

37
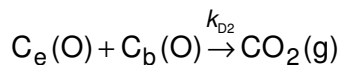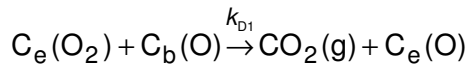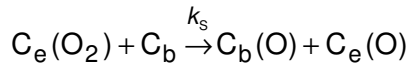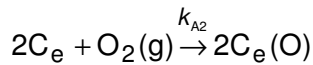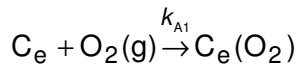
Fig. 6 (a) An Arrhenius plot of SCPM data for the five experimental oxygen isobars. (b) A plot of the effects of oxygen partial pressure and temperature on ak"$_{eff}$. The reaction rate constants are plotted relative to ak"$_{eff}$ (T, 40 kPa). (c) A ln–ln plot of carbon flux vs. oxygen concentration. The shaded regions represent the two-sided 95% confidence interval for the linear fits at each temperature. The slopes from each isothermal set are plotted in (d) to show the change in effective reaction order with temperature. The shaded region and dotted line represent the two-sided 95% confidence intervals for the linear fit and the individual data points, respectively. The error bars in all subplots represent two-sided 95% confidence intervals about the sampled mean.
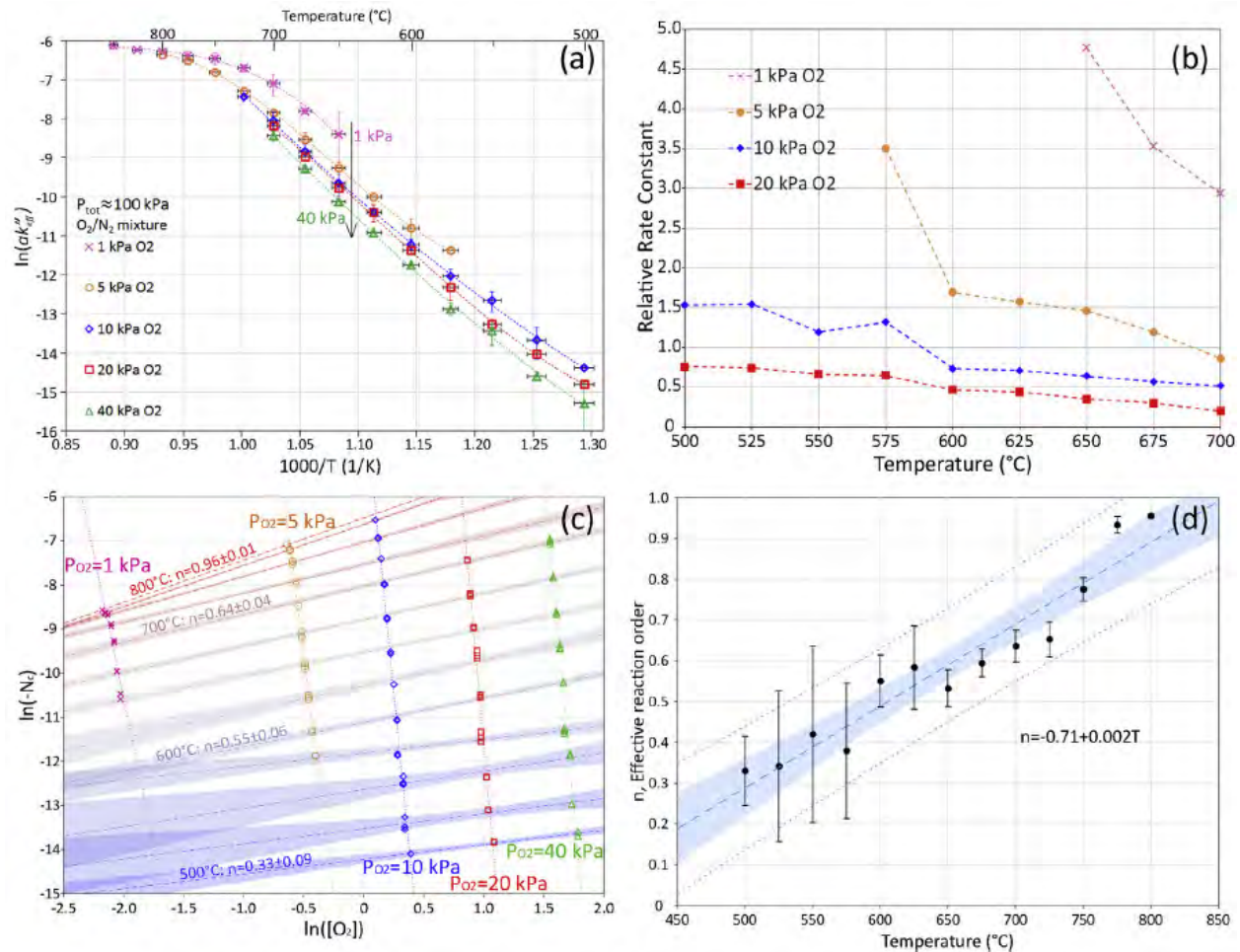
The most obvious simplifications to the oxygen transfer mechanism are the removal of surface diffusion hopping, $C_{b1}(O) \leftrightarrow C_{b2}(O)$, and nascent site deactivation (NSD), $2C_e \leftrightarrow 2C_b$. The mobility of $C_b(O)$ on the basal plane is quite high. It was assumed that the resistance to oxygen diffusion was much smaller than that of the adsorption or desorption processes and consequently not a rate-limiting factor. NSD was neglected to simplify the mathematical complexity and eliminate the need to track each individual reaction site. Additionally, complete conversion can be achieved; therefore, site deactivation must eventually reverse.

The relationship between the rate of oxygen adsorption, molecular oxygen chemisorptions, oxygen dissociative chemisorptions, and NSD is indeed complex. Jones *et al.* [65], estimated ring closure to occur one order of magnitude faster than the maximum rate of oxygen adsorption; yet it was also stated that "a point may be reached when ring contraction would no longer be favored because of steric hindrance". This point could be the result of graphite becoming increasingly strained to accommodate further ring closure or due to the presence of

oxygen complex on the surface [65,66]. Radovic *et al.* [35] used density functional theory (DFT) simulations to compare the deactivation of adjacent zigzag sites. When four adjacent active sites were modeled, ring closure occurred. When only two adjacent sites were modeled, ring closure did not occur due to the need for a substantial driving force; thus, further oxidation of the nascent sites would be expected.

Site anisotropy was also eliminated from the OTM; consequently, all reactive sites are considered equivalent. Silva-Tapia *et al.* [36] showed that molecular-oxygen and oxygen-dissociative are the major pathways for molecular and dissociative chemisorption, respectively; however, equal treatment of the carbene and carbyne type active sites greatly reduces the mathematical complexity, allowing an average intrinsic rate to be derived explicitly in terms of temperature and gaseous oxygen concentration. This simplification allows the general effects of these types of chemisorptions to be observed without the need for an implicit solution to the intrinsic rate equation.

Oxygen transfer model derivation
The gaseous carbon flux outward from the graphite surface may be written out concisely as

$$-N_c = k_{D1}^*[C_e(O_2)] + \left(k_{D2}^* + k_{D3}\right)[C_e(O)]$$

Unfortunately, this equation is of limited practical use in many cases because the surface concentrations, $[C_e(O)]$ and $[C_e(O_2)]$, are not easily determined. The surface concentrations can be determined for the OTM using the law of mass action to apply a differential mass balance about C_e, $C_e(O)$, and $C_e(O_2)$. It was assumed that the total number of edge sites per unit area of the {100} and {110} surfaces was constant. This allowed an edge-site conservation equation

$$\Gamma_e = [C_e] + [C_e(O_2)] + [C_e(O)]$$

to be invoked and used directly to account for $[C_e]$. For the concentration of available sets of C_e sites, $[2C_e]$, it was assumed that

$$|2C_e| \sim \tfrac{1}{2}\left(\Gamma_e - [C_e(O_2)] - [C_e(O)]\right)$$

It should be noted that many of the reactions are not truly elementary reactions. It is assumed in all cases that these reactions have one transition state with a significantly larger energy barrier than other transition states within the reaction pathway. Consequently, the single largest transition-state barrier dictates the rate of reaction. This fact was demonstrated via DFT by Orrego *et al.* [42] Furthermore, a pseudo-steady-state is assumed. Upon extensive algebraic manipulation and rearrangement $[C_e(O)]$ and $[C_e(O_2)]$ may be explicitly written in terms of the experimentally-determined Arrhenius parameters, temperature, and the gaseous oxygen concentration at the gas–solid interface.

After substitution of the expressions for $[C_e(O)]$ and $[C_e(O_2)]$ and considerable rearrangement, N_c can be redefined as

$$-N_c(T,[O_2]) = \frac{\left(k_{A1}k_{D1}^* + (k_{A1} + k_{A2})\left(k_S^* + k_{D1}^*\right)\right)\left(k_{D2}^* + k_{D3}^*\right)\Gamma_e[O_2]}{(k_{A1} + k_{A2})\left(k_S^* + k_{D1}^*\right)[O_2] + \left(k_{A1}[O_2] + k_S^* + k_{D1}^*\right)\left(k_{D2}^* + k_{D3}\right)}$$

Comparing the two expressions for N_c reveals that ak''_{eff} is a function of gaseous oxygen concentration as well as temperature, where

$$ak''_{eff}(T,[O_2]) = \frac{\left(k_{A1}k^*_{D1} + (k_{A1} + k_{A2})(k^*_S + k^*_{D1})(k^*_{D2} + k^*_{D3})\right)\Gamma_e}{(k_{A1} + k_{A2})(k^*_S + k^*_{D1})[O_2] + \left(k_{A1}[O_2] + k^*_S + k^*_{D1}\right)(k^*_{D2} + k_{D3})}$$

Oxygen transfer model fit to experimental data
This equation was used as a basis for the estimation of the rate constants of the above-listed reactions. All reaction-rate constants were assumed to have an Arrhenius temperature dependence of the form $k_i(T) = k_{oi}\exp(-E_i/RT)$. Data comparing the fit of the OTM for the estimated parameters are given in Table 2. The parameters k_{oi} and E_i are listed in Tables 3 through 5 for the optimization of all isobars, 1–10 kPa O_2, and 10–40 kPa O_2, respectively.

Table 2 indicates a "good" fit between the experimental results and the OTM. In the experimental temperature and O_2 partial pressure range used, the model's predicted effective reaction rate constant is off by no more than a factor of 2.6. The fit of the 1, 5, and 10 kPa isobars (Table 4) produces the smallest overall residual error between model and experimental data. A plot of the optimized model for 1, 5, and 10 kPa data is given in Fig. 7a. The OTM predicts the majority of the fitted data well with the exceptions of oxygen partial-pressure data for 1 kPa below 700 °C and 20 and 40 kPa data above 600 °C. As seen in the residual-error plot in Fig. 7b, the magnitude of the residual error correlates roughly with the variation in partial pressure and the error is largest between 600 and 700 °C.

Table 2   All values are reported as absolute relative error between model and experimental data. The average, standard deviation, and maximum residual error are tabulated to show the effect of the three optimizations (all isobars, 1–10 kPa isobars, and 10–40 kPa isobars) on the residual error for each individual isobar as well as the entire set of experimental data.

Fit Statistics (%)	All			1, 5, 10			10, 20, 40		
	Avg.	St. Dev.	Max.	Avg.	St. Dev.	Max.	Avg.	St. Dev.	Max.
All	35	38	156	26	21	86	39	33	132
1 kPa	31	45	156	19	25	86	49	18	61
5 kPa	65	50	140	14	9	32	66	37	132
10 kPa	49	27	93	9	6	23	54	29	96
20 kPa	9	7	24	38	11	57	16	10	34
40 kPa	18	9	32	52	10	62	10	8	26

Table 3   Resulting parameters of nonlinear optimization for all experimental isobars. Activation energies are given in kJ/mol.

k_i	k_{A1} [m^3/mol.s]	k_{A2} [m^3/mol.s]	k_S^* [s^{-1}]	k_{D1}^* [s^{-1}]	k_{D2}^* [s^{-1}]	k_{D3} [s^{-1}]
k_{oi}	2.82x10^3	3.45x10^3	4.51x10^6	9.92x10^8	3.26x10^8	1.75x10^{16}
E_i	86	34	137	210	147	273

Table 4   Resulting parameters of nonlinear optimization for the 1, 5, and 10 kPa isobars. Activation energies are given in kJ/mol.

k_i	k_{A1} [m^3/mol.s]	k_{A2} [m^3/mol.s]	k_S^* [s^{-1}]	k_{D1}^* [s^{-1}]	k_{D2}^* [s^{-1}]	k_{D3} [s^{-1}]
k_{oi}	2.09x10^3	1.80x10^3	9.02x10^7	8.21x10^8	3.31x10^8	4.46x10^{16}
E_i	71	28	113	200	148	289

Table 5 Resulting parameters of nonlinear optimization for the 10, 20, and 40 kPa isobars. Activation energies are given in kJ/mol.

k_i	k_{A1} [m³/mol.s]	k_{A2} [m³/mol.s]	k_S^* [s⁻¹]	k_{D1}^* [s⁻¹]	k_{D2}^* [s⁻¹]	k_{D3} [s⁻¹]
k_{oi}	2.58×10^3	1.66×10^3	7.27×10^7	1.05×10^9	3.86×10^8	4.05×10^{16}
E_i	100	34	90	175	148	278
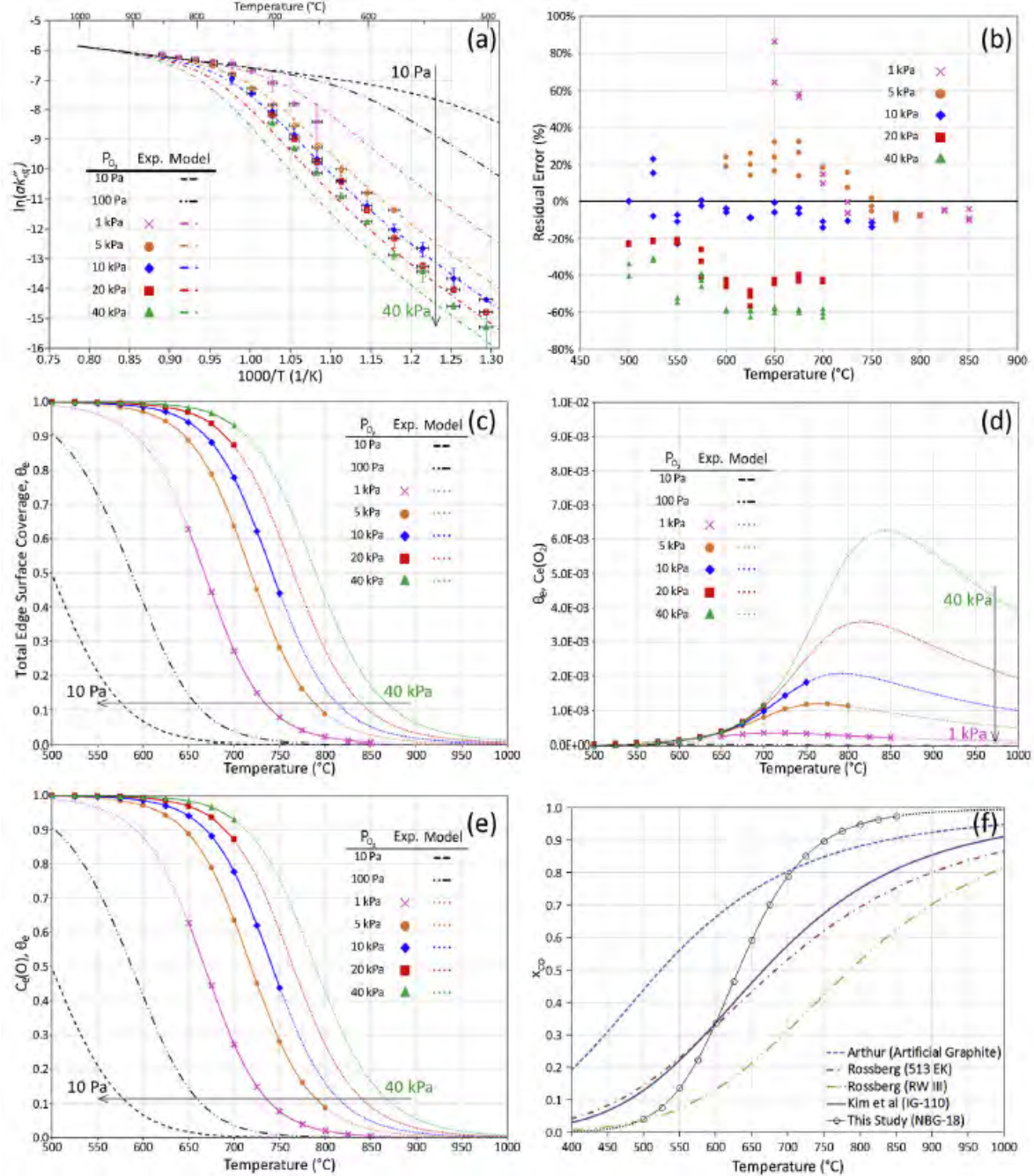
Fig. 7 Results from the OTM (a) compares ak''_{eff} of the experimental and fitted OTM using parameters from Table 4. The residual error between the experimental values and the OTM is shown in (b). The total surface complex coverage of the edge planes, (denoted θ_e) is shown in (c), whereas (d) and (e) show the surface coverage of the individual reactive surface complexes $Ce(O_2)$ and $Ce(O)$, respectively, and (f) shows the fractional carbon conversion to gaseous CO predicted by the OTM compared to empirical fits of experimental data for various carbon materials [17,78,79].

Oxygen transfer model validation

As shown in Fig. 7a, the OTM describes the observations made regarding the effective reaction rate constant. The low-, intermediate-, and high-temperature regions correspond approximately with activation energies for the indirect desorption of CO_2, direct desorption of CO, and the dissociative chemisorption of oxygen, respectively. The OTM also accounts for the increase in ak''_{eff} with decreasing oxygen partial pressure, the decreasing difference between the values of ak''_{eff} with increasing temperature, and the experimentally observed temperature dependence of the effective reaction order. While a good fit to experimental observations is important, it does little to validate the accuracy of the individual reactions implied within the model. To validate the model, the fitted parameters for each reaction pathway are compared to available literature as well as key literature observations.

As is the case with much of the carbon oxidation literature, the range of values for the kinetics of oxygen adsorption on carbon is quite broad. Activation energies for adsorption of oxygen range from 0 to approximately 130 kJ/mol [34,36,61,80–83]. Bansal *et al.* [82] observed five distinct chemisorptions processes with increasing surface coverage for activated Graphon between -78° and 160 °C. The activation energies ranged from approximately 13 kJ/mol to 52 kJ/mol for low and high surface coverage, respectively. In a much later study, TGA/DSC was used to study the chemisorption of oxygen on Saran chars at 100 kPa between 77° and 222 °C to yield an activation energy of 47.7 ± 2.9 kJ/mol for surface coverage between 0.76 and 0.96 [81]. The activation energy for dissociative chemisorption of oxygen in the OTM falls right in the middle of this range. As seen in Fig. 7c–e θ_e varies both with temperature and pressure. Higher equilibrium θ_e is maintained for greater oxygen partial pressures. The OTM implicitly assumes that reaction rate constants are independent of surface coverage and surface-species interactions.

Comparisons of the optimized parameters for 1, 5, and 10 kPa O_2 and 10, 20, and 40 kPa do show an increase in activation energies for the adsorption processes which may result from differences in the average θ_e for the optimizations. Silva-Tapia *et al.* [36] used DFT simulations to show that the dissociative chemisorption of oxygen should occur on the carbine type armchair sites with an activation energy of approximately 3 kJ/mol for carbon nanotubes and 28 kJ/mol for graphene. For molecular chemisorption, Radovic *et al.* [34,36] predicted activation energies between 71 and 80 kJ/mol on carbene type zigzag sites for carbon nanotubes and graphene, respectively. These calculations did not consider the effects of surface complexes on the edge or basal planes. Values found in the remaining literature for the chemisorption of oxygen range from 54 to 134 kJ/mol. Kelemen *et al.* [61] found using Auger electron spectroscopy activation energies ranging from 54 to 134 kJ/mol, respectively, for θ_e ranging from 0.2 to 0.9, respectively. Finally, Walker *et al.* [80], using thermoelectric power measurement on pressed bars of high-purity graphite flakes, measured an activation energy of 125 ± 8 kJ/mol for temperatures between 327° and 452 °C and an oxygen partial pressure of 100 kPa. No significant variation of the activation energy was found with the reported quantities of adsorbed oxygen. From Fig. 7c it is expected that the surface coverage would be quite high throughout the experimental range. Walker [80] also reported a pre-exponential factor equivalent to 2:2 x 10^3 m^3/mol s.

To the best of the authors' knowledge an activation energy for the spill-over of oxygen to the basal plane has not been measured experimentally; however, Radovic *et al.* [57] estimated the activation energy to overcome the transition state between the reactant and products side of:

$$C_e(O_2) + C_b \xrightarrow{k_s} C_b(O) + C_e(O)$$
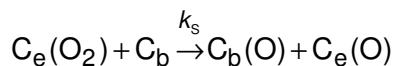
to be approximately 130 kJ/mol using DFT. The parameter optimizations in Tables 4 and 5 result in slightly lower activation energies of approximately 110 and 90 kJ/mol, respectively. A decrease in the activation energy is observed between Tables 4 and 5; however, this observation does not necessarily imply a decrease in the activation energy with increasing surface-complex concentrations, as the difference is likely within the range of experimental uncertainty. Further experimental work and DFT simulations should be used to make such an inference.

Literature for the desorption of CO_2 and CO from the active surface area is quite abundant. Experimentally it has been shown that the activation energy for surface-complex removal decreases with increasing surface coverage [37,39,77]. Tables 4 and 5 show a decrease in the optimized activation energy for direct CO_2 and CO adsorption at higher average surface coverage. DFT has also suggested that desorption energies are substantially lowered (~30% decrease) by the presence of the epoxide on the basal plane. These facts, at least in part, can account for the broad range of observed activation energies. For CO_2 desorption, activation energies range from approximately 120 to 250 kJ/mol for high and low surface coverage, respectively [61,76,77]. Orrego *et al.* [42] determined for indirect CO_2 desorption an activation energy of approximately 145 kJ/mol. The proposed energy barrier is due to the rearrangement of the seven-member ring after oxygen insertion (unzipping) into a four-membered ring lactone group subsequent to desorption. The optimized activation energy from Tables 4 and 5 is 148 kJ/mol. A proposed reaction pathway for direct CO_2 desorption was estimated via DFT to have an activation energy of 203 kJ/mol [43]. The presence of $C_b(O)$ on the basal plane is critical for the decomposition, as the activation energy would otherwise be significantly higher. The molecular-beam study by Olander *et al.* [59] suggested that at 1177 °C the direct production route for CO_2 should account for 80–90% of the total evolved CO_2. The OTM at this same temperature predicts approximately 80% of CO_2 will be formed via the direct path.
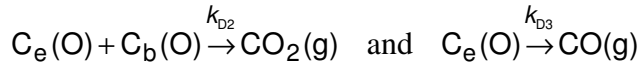
Activation energies for CO desorption in the literature generally range from 240 kJ/mol at high surface coverage to 350 kJ/mol at low surface coverage [28,61]. The kinetics of desorption for CO via a semiquinone carbon–oxygen complex determined via DFT in the absence of other functional groups yielded an activation energy of 396 kJ/mol and a pre-exponential factor of 1.81 x 10^{17} s^{-1}. This pre-exponential factor is in good agreement with the optimized values in Tables 2–4. If a stable surface complex is assumed to be near the $C_e(O)$ complex, assuming a 30% reduction in the carbon–carbon bond energy and equivalent reduction in the activation energy for desorption, the activation energy would be closer to 280 kJ/mol. This value is comparable to that of the optimized OTM.

The OTM is also capable of predicting the CO/CO_2 ratio:

$$\frac{CO}{CO_2} = \frac{k_{D3}(k_{A1} + k_{A2})\left(k_S^* + k_{D1}^*\right)}{k_{A1}k_{D1}^*\left(k_S^* + k_{D1}^*\right) + k_{D2}^*(k_{A1} + k_{A2})\left(k_S^* + k_{D1}^*\right)}$$

Although no experimental data were collected for the product ratio, the model fits reasonably with other published literature shown in Fig. 7f. The experimental values for the CO/CO_2 ratio are often fitted empirically to an Arrhenius model. Values of the empirical activation energy vary significantly depending on the experimental conditions. Phillips *et al.* [84,85] reported an empirical value of approximately 27 kJ/mol for oxygen partial pressures between approximately

1 and 27 Pa and temperatures ranging from 525 to 625 °C. Arthur [78] found that for both a natural graphite and a coal char (460–900 °C and oxygen partial pressures of 5–25 kPa) the empirical activation energy was 51 kJ/mol. Rossberg [79], for two electrode carbons (520–1420 °C), found somewhat higher values of 60 and 78 kJ/mol. Kim *et al.* [17] reported an activation energy of approximately 70 kJ/mol for temperatures between 950 and 1800 °C and oxygen partial pressures varying between 5 and 20 kPa. The flows used in these experiments, with the exception of that of Phillips [84], were well below the velocity of approximately 51 m/s needed to prevent secondary oxidation of CO [84]. Additionally, reactions between the CO and the reactive surface complexes may have occurred, artificially decreasing the CO/CO_2 ratio. The empirical activation energy resulting from the OTM using the optimized parameters from Table 4 results is 141 kJ/mol. Examination of Table 4 shows that the activation energy is the difference between the activation energies for reactions

$$C_e(O) + C_b(O) \xrightarrow{k_{D2}} CO_2(g) \quad \text{and} \quad C_e(O) \xrightarrow{k_{D3}} CO(g)$$

suggesting, as in much of the literature, that the empirical activation energy is related to the energy difference for desorption of CO and CO_2. Upon analysis of the terms in the numerator and denominator of the CO/CO_2 equation, the following simplification is realized over the temperatures and oxygen concentrations of the experimental data:

$$\frac{CO}{CO_2} \sim \frac{k_{D3}}{k_{D2}^*}$$

Neither expression for the CO/CO_2 ratio has any direct dependence on the oxygen concentration within the system. Phillips *et al.* [85] showed that the amount of stable complex formed, $C_b(O)$, was strongly dependent on the initial oxygen concentration within the system, and the product ratio decreased with increasing oxygen concentration. This observation suggests that the product ratio is a function of the concentration of $C_b(O)$ on the basal plane. Noting that $k_{D2}^* = k_{D2}[C_b(O)]$,

$$\frac{CO}{CO_2} \sim \frac{k_{D3}}{k_{D2}[C_b(O)]}$$

which is of the same form as the expression derived by Skokova *et al.* [86] for an early form of the oxygen transfer mechanism. Intuitively, an increase in the system's oxygen concentration should increase the concentration of the stable oxygen complex on the basal plane, which agrees with the findings of Phillips [85]. The degree to which the concentration of the stable surface complex increases is also dependent upon the equilibrium rate of consumption of the complex.

Oxygen transfer model deficiencies
The OTM fits the experimental kinetics data, and the optimized parameters agree well with literature for the corresponding reaction pathways used; however, there are some deficiencies within the model. The first is the failure to predict changes in the product ratio with changing oxygen concentration. The change in product ratio may be accounted for in the model by dropping the simplification of k_S, k_{D1}, and k_{D2} to k_S^*, k_{D1}^*, and k_{D2}^* and using an implicit method to solve for the conservation equations for the five surface species. In addition, careful consideration must be given to the concentration of the epoxide on the basal plane bearing in

mind that it is only consumed at the edge. Skokova *et al.* [86] observed an inverse proportionality between the product ratio and the crystallite size, which could suggest that, at least for "small" cyrstallites, the migration of stable complex on the basal plane must be taken into consideration, as its (in)ability to diffuse away from the crystallite edge will affect the concentration near the RSA.

Another deficiency is the failure to account for the known dependency of reaction parameters on surface coverage. Although Tables 4 and 5 do show the correct general trends of the reaction parameters for the lower and higher "average" surface coverage, the optimized parameters only reflect an average value rather than the actual value throughout the fitted range of experimental data. Accounting for this dependency may eliminate a majority of the experimental residual error. The dependency may be added to the activation energies as a correction factor that varies with θ_e. This method should decrease the residual error but has no physical meaning.

Next, it is assumed in the model derivation that $|2C_e| \sim \frac{1}{2} (\Gamma_e - [C_e(O_2)] - [C_e(O)])$ suffices to describe the concentration of available sites for dissociative chemisorptions of oxygen. This assumption is expected to be a good approximation at low to moderate surface coverage. At high surface coverage, it may become increasingly inaccurate. Although dissociative chemisorption is expected to occur nearly exclusively on the carbyne type armchair sites, the model assumes no site specificity. The lack of site specificity makes each individual carbon edge site a potential adsorption site and near the maximum surface coverage, the assumption will not describe the availability of edge site pairs, which may in part explain the lack of conformity of the OTM with the high-pressure studies of Ranish *et al.* [64]. At the temperatures and pressures of those experiments, the OTM predicts that the reaction is nearly independent of oxygen concentration, whereas the experimental data of Ranish *et al.* [64] show an increase in the reaction order with decreasing oxygen partial pressure.

Finally, the OTM assumes that the maximum achievable concentration of edge surface complex is Γ_e, which was set to 2.01 x 10^{-5} mol/m^2, the average of the ideal (100) and (110) planar densities. On the nano-scale this appears to be a valid assumption given the atomic level smoothness observed in the micrographs of Fig. 8; however, the assumption that all carbon sites are equally available as potential reaction sites may be questionable.
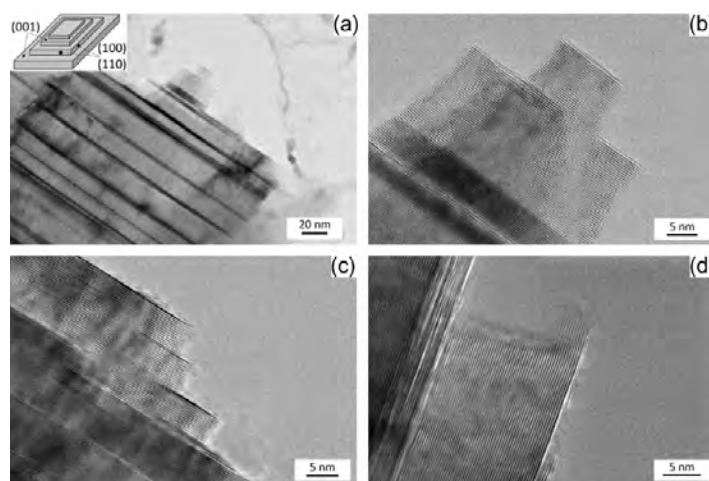

Fig. 8   High-resolution TEM micrographs of NBG-18. The reaction progression along the edge-plane steps appears uniform; (a) the terracing commonly observed in large crystallites within the filler particles; (b) the tip of the crystallite from (a); (c and d) the terracing at the edges of crystallites.

References

1. Tarpinian, A, Gazza, GE, A technique for the microstructural examination of polycyrstalline graphites. Report WAL-TR-132.5/1. Watertown Arsenal Laboratory; February 1959.
2. Walker Jr PL, Rusinko F, Austin LG. Gas reactions of carbon. In: Eley DD, Selwood PW, Weisz PB, editors. Advances in catalysis, vol. 11. New York: Academic Press; 1959. p. 133–221.
3. Radovic LR. Carbon and graphite reactivity. In: Buschow KHJ, Cahn RW, Flemings MC, Ilschner B, Kramer EJ, Mahajan S, editors. Encyclopedia of materials: science and technology. New York: Elsevier; 2001.
4. Lambert JD. The effect of certain metals on the oxidation process of carbon. Trans Faraday Soc 1936;32:1080–3.
5. Allardice DJ, Walker Jr PL. The effect of substitutional boron on the kinetics of the carbon–oxygen reaction. Carbon 1970;8:375–85.
6. ASTM Standard D7219, 2008. Standard specification for isotropic and near isotropic nuclear graphites. West Conshohocken (PA): ASTM International; 2003. http://dx.doi.org/10.1520/D7219-08.
7. Ranish JM. Kinetics of the carbon–oxygen reaction. Penn State Univ, PhD Thesis. University Park, PA, USA; 1984.
8. Nelder JA, Mead R. A simplex method for function minimization. Comput J 1965;7:308–13.
9. Levenspiel O. Chemical reactor omnibook. Corvallis (OR): OSU Book Stores Inc.; 1996. p. 51.1–55.25.
10. Levenspiel O. Chemical reaction engineering. 3rd ed. Hoboken (NJ): John Wiley & Sons Inc.; 1999. p. 567–586.
11. Laine NR, Vastola FJ, Walker Jr PL. The importance of active surface area in the carbon oxygen reaction. J Phys Chem 1963;67:2030–4.
12. Szekely J, Evans JW, Sohn HY. Gas–solid reactions. New York: Academic Press; 1976.
13. White DE, Carberry JJ. Kinetics of gas–solid non-catalytic reactions. Can J Chem Eng 1965;43:334–7.
14. Shen J, Smith JM. Diffusional effects in gas solid reactions. Ind Eng Chem Fund 1955;4:293–310.
15. Svehla RA. Estimated viscosities and thermal conductivities of gases at high temperatures. Technical Report R-132, NASA; 1962.
16. Parker AS, Hottel HC. Combustion rate of carbon study of gas-film structure by microsampling. Ind Eng Chem 1936;28:1334–41.
17. Kim ES, No HC. Experimental study on the oxidation of nuclear graphite and development of an oxidation model. J Nucl Mater 2006;349:182–94.
18. Yang H, Eun H, Lee D, Jung C, Lee K. Analysis of combustion kinetics of powdered nuclear graphite by using a nonisothermal thermogravimetric method. J Nucl Sci Technol 2006;43:1436–9.
19. Kawakami H. Air oxidation behavior of carbon and graphite materials for HTGR. Tanso 1994;124:26–33.
20. Chi S, Kim G. Comparison of oxidation rate and degree of graphitizaition of selected IG and NBG nuclear grades. J Nucl Mater 2008;381:9–14.
21. Kim ES, No HC, Kim BJ, Oh CH. Estimation of graphite density and mechanical strength variation of VHTR during air-ingress accident. Nucl Eng Des 2008;238(4):837–47.
22. Xiaowei L, Jean-Charles R, Suyuan Y. Effect of temperature on graphite oxidation behavior. Nucl Eng Des 2004;227(3):273–80.

23. Hinssen HK, Ku¨hn K, Moorman R, Schlo¨gl B, Fechter M, Mitchell M. Oxidation experiments and theoretical examinations of graphite materials relevant for the PBMR. Nucl Eng Des 2008;238(11):2018–3025.

24. Moormann R, Hinssen HK, Ku¨hn K. Oxidation behavior of an HTR fuel element matrix graphite in oxygen compared to a standard nuclear graphite. Nucl Eng Des 004;227:281–4.

25. Fuller EL, Okoh JM. Kinetics and mechanisms of the reaction of air with nuclear grade graphites: IG-110. J Nucl Mater 1997;240:241–50.

26. Ahmed S, Back MH. The role of the surface complex in the kinetics of the reaction of oxygen with carbon. Carbon 1985;23:513–24.

27. Radovic LR. Active sites in graphene and the mechansim of CO_2 formation in carbon oxidation. J Am Chem Soc 2009;131:17166–75.

28. Radovic LR, Silva-Villalobos AF, Silva-Tapia AB, Vallejos-Burgos F. On the mechanism of nascent site deactivation in graphene. Carbon 2011;49:3471–87.

29. Silva-Tapia AB, Garcı´a-Carmona X, Radovic LR. Similarities and differences in O_2 chemisorption on graphene nanoribbon vs. carbon nanotube. Carbon 2012;50:1152–62.

30. Jones JM, Jones DH. Modelling the competition between annealing and oxidation in the carbon–oxygen reaction. Carbon 2007;45(3):677–80.

31. Senneca O, Salatino P, Sabato M. The influence of char surface oxidation on thermal annealing and loss of carbon reactivity. Proc Combust Inst 2005;30:2223–30.

32. Orrego JF, Zapata F, Truong TN, Mondrago´n F. Heterogeneous CO_2 evolution from oxidation of aromatic carbon-based materials. J Phys Chem A 2009;113:8415–20.

33. Arthur JR. Reactions between carbon and oxygen. Trans Faraday Soc 1951;47:164–78.

34. Rossberg VM. Experimentelle Ergebnisse uber die Primarreaktionen bei der Kohlenstoffverbrennung. Z Elektrochem 1956;60:952–6.

35. Kelemen SR, Freund H. O_2 oxidation studies of the edge surface of graphite. Carbon 1985;23:619–25.

36. Walker Jr PL, Austin LG, Tietjen JJ. Oxygen chemisorptions effects on graphite thermoelectric power. In: Walker Jr PL, editor. Chemistry and physics of carbon, vol. 1. New York: Dekker; 1965. p. 327–65.

37. Ismail IMK, Walker Jr PL. Detection of low temperature gasification using DSC and TGA. Carbon 1989;27(4):549–59.

38. Bansal RC, Vastola FJ, Walker Jr PL. Studies on ultraclean carbon surfaces: II. Kinetics of chemisorption of graphon. J Colloid Interface Sci 1970;32(2):187–94.

39. Sendt K, Haynes BS. Density functional study of the chemisorption of O_2 on the zig-zag surface of graphite. Combust Flame 2005;143:629–43.

40. Radovic LR, Silva-Tapia AB, Vallejos-Burgos F. Oxygen migration on the graphene surface. 1. Origin of epoxide groups. Carbon 2011;49(11):4218–25.

41. Vastola FJ, Hart PJ, Walker Jr PL. A study of carbon–oxygen surface complexes using O^{18} as a tracer. Carbon 1964;2(1):65–71.

42. Skokova K, Radovic LR. On the role of carbon–oxygen surface complexes in the carbon/oxygen reaction mechanism. Washington (DC): American Chemical Society (Div. Fuel Chem. Pre-prints) ACS; 1996. p. 143–7.

43. Sánchez A, Mondragón F. Role of the epoxy group in the heterogeneous CO_2 evolution in carbon oxidation reactions. J Phys Chem C 2007;111:612–7.

44. Olander DR, Jones RH, Schwarz JA, Siekhaus WJ. Reactions of modulated molecular beams with pyrolytic graphite. II. Oxidation of the prism plane. J Chem Phys 972;57:421–33.

45. Marchon B, Carrazza J, Heinemann H, Somorjai GA. TPD and XPS studies of O_2, CO_2 and H_2O adsorption on clean polycrystalline graphite. Carbon 1988;26(4):507–14.

46.   Phillips R, Vastola FJ, Walker Jr PL. Factors affecting the product ratio of the carbon–oxygen reaction – II. Reaction temperature. Carbon 1970;8:205–10.
47.   Phillips R, Vastola FJ, Walker Jr PL. The effect of oxygen pressure and carbon burn-off on the product ratio of the carbon–oxygen reaction. Carbon 1969;7:479–85.
48.   Skokova K, Radovic LR. CO/CO_2 ratio in the products of the carbon–oxygen reaction. In: Proceedings of the 22nd biennial conference on carbon. San diego (CA): American Carbon Society; 1995. p. 608–9.
49.   Ranish JM, Walker Jr PL. High pressure studies of the carbon–oxygen reaction. Carbon 1993;31(1):135–41.

Microstructure of Neutron-Irradiated Graphite

Summary
Graphite subject to low-dose (1.5 – 2 dpa) neutron irradiation showed no evidence of shrinkage along the *c*-axis or the associated closing of micro-cracks; however, both phenomenon were readily observed in samples irradiated to ~6.7 dpa. While filler particles in such samples still showed the presence of numerous cracks, the binder phase and QI particles were highly densified, containing almost no residual micro-cracks. As in earlier work on electron-irradiated graphite, evidence was found of prismatic dislocation dipoles and vacancy loops, again suggesting that positive climb resulting in the formation of new basal planes is responsible for irradiation-induced swelling. Unlike under electron irradiation, graphite under neutron irradiation largely retains an intact lattice structure due to the increased temperature of the irradiation treatment.

Experimental Details
Nuclear graphite samples of several different grades were irradiated as a part of the advanced creep capsule (AGC-1) experiment at the Advanced Test Reactor National User Facility (ATR-NSUF). TEM specimens were prepared out of the piggy-back samples which were irradiated in an un-loaded condition. The details of the samples used for microstructure characterization are provided in Table 1. Initial cutting and polishing of the TEM specimens were performed at the Center for Advanced Energy Studies (CAES) and the final sample mounting, ion-beam thinning and TEM studies were carried out Boise State.

Table 1   Irradiation conditions of various graphite grades used for microstructural characterization

Grade	Loading Location	Dose (dpa)	Temperature (^{o}C)
IG-110	2PB23	1.91	451
IG-110	1PB21	6.70	674
NBG-18	1PB25	1.54	430
NBG-18	1PB18	6.78	678
PCEA	1PB24	1.78	440
PCEA	1PB17	6.81	679

Results

Low dpa (1.5 to 2 dpa) samples
Bright field TEM micrographs recorded from NBG-18 sample irradiated to 1.54 dpa are shown in figure 1. Fig. 1(a) shows the microstructure of the binder region with embedded QI particles. The QI particles are very similar in shape and size to those observed in the non-irradiated graphite samples. Fig. 2(b) shows the microstructure of a filler particle. In both the binder and filler regions, one can see the presence of numerous micro and nanometer sized shrinkage cracks. These micrographs do not show any evidence for the irradiation-induced shrinkage of graphite along the *c*-axis and associated closing of micro-cracks. It is possible that the dimensional change is not significant enough to be seen under TEM. The microstructures of the other grades of graphite irradiated under similar conditions are very similar and show no significant irradiation-induced changes.
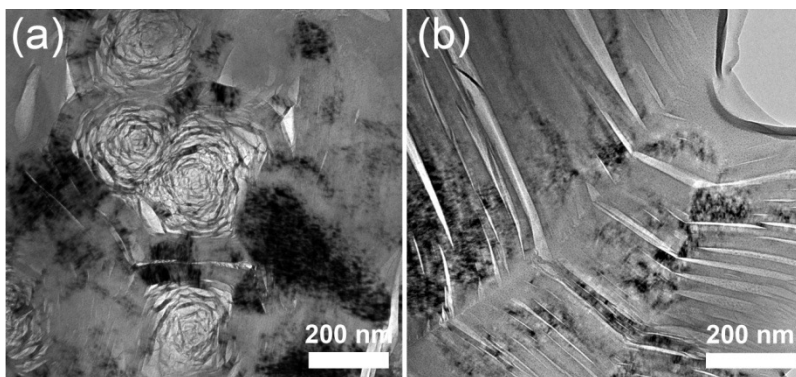
Fig. 1 Bright-field micrographs recorded from (a) binder and (b) filler regions of NBG-18 graphite irradiated to 1.54 dpa.

High dpa (~6.7 dpa) samples
Fig. 2 shows the bright-field micrographs recorded from the filler regions of NBG-18 graphite irradiated to 6.78 dpa. Fig. 1(a) shows a filler particle with numerous microcracks similar to the ones present in non-irradiated graphite; however, Fig. 2(b) recorded from a different filler particle shows a complete absence of microcracks, indicating a substantial swelling of the graphite particle along the *c*-axis. The filler particles throughout the sample showed a varying degree of *c*-axis swelling and crack-closing. The bright-field images of the filler particles that show crack-closing also show the presence of significant structural disorder, which is evident from the diffraction contrast in Fig. 2(b).
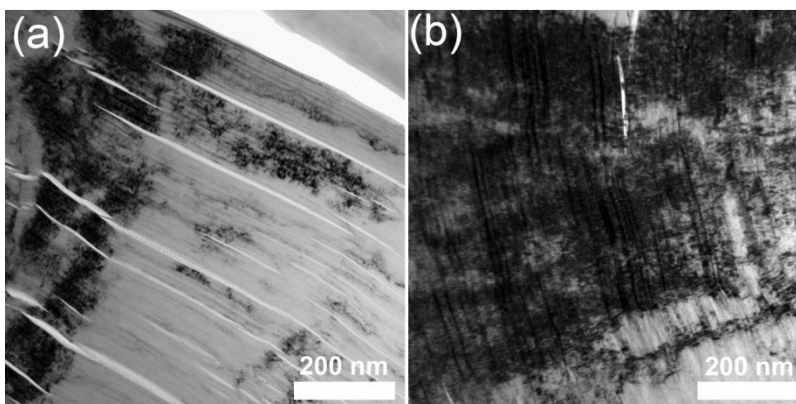

Fig. 2 Bright-field micrographs recorded from the filler regions of NBG-18 graphite irradiated to 6.78 dpa.

The most striking effect of irradiation was seen in the binder region. Fig. 3 shows a typical micrograph recorded from the binder region with embedded QI particles. It can be seen clearly that the binder region looks highly densified with almost no residual micro-cracks. This type of densification of binder is seen throughout the sample. The QI particle shown in Fig. 3(b) shows the complete transformation of a QI particle from a rosette with concentric graphite strands to a highly densified solid sphere. It is interesting to note that the micrographs from the binder regions show almost complete densification without much open space left, whereas the filler particles still show the presence of numerous cracks. One explanation might be that graphite particles in the binder are smaller and randomly oriented, leading to a uniform swelling/densification in all directions. It will be interesting to see the effect of this dissimilarity in the densification between the various microstructural features on the physical properties of

50

these graphites. The other two grades (IG-110 and PCEA) under study also showed a very similar densification behavior.
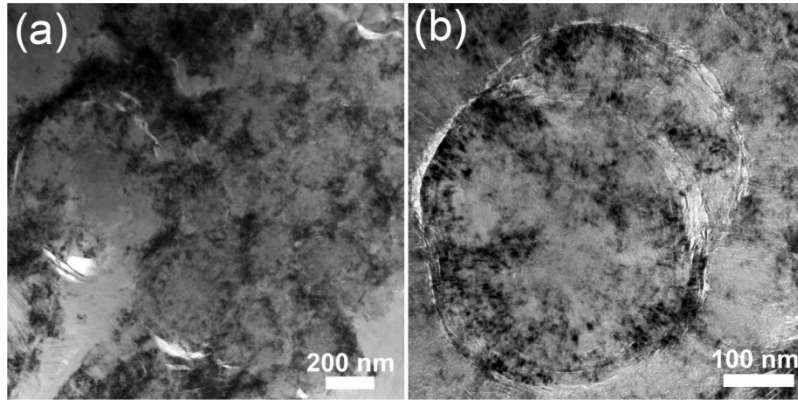

Fig. 3   Bright-field micrographs recorded from the binder regions of NBG-18 graphite irradiated to 6.78 dpa.

Fig. 4 shows the lattice images recorded along a direction normal to [001] and depicts the basal planes of NBG-18 graphite irradiated to 6.78 dpa. The micrograph in Fig. 4(a) clearly shows the presence of breaking and bending of lattice planes caused associated with dislocations. Fig. 4(b) shows a part of figure 4(a) magnified and noise-filtered. It shows the presence of dislocation dipoles as well as evidence for the positive climb of these prismatic dislocations leading to the creation of extra basal planes. We have noticed a few vacancy loops, but no interstitial loops. These findings are identical to those of our earlier work on in-situ electron-beam irradiated graphites, where the irradiation-induced swelling was attributed mainly to the positive climb of prismatic dislocations resulting in the formation of new basal planes. The same mechanism can be used to explain the swelling in neutron-irradiated graphite; however, unlike for electron-irradiation, most of the graphite lattice is still intact even after undergoing a damage of about 6.7 dpa. The largely ordered structure is retained because the neutron-irradiation was carried out at much higher temperatures (Table 1), giving enough thermal energy for the point defects to migrate and anneal out.
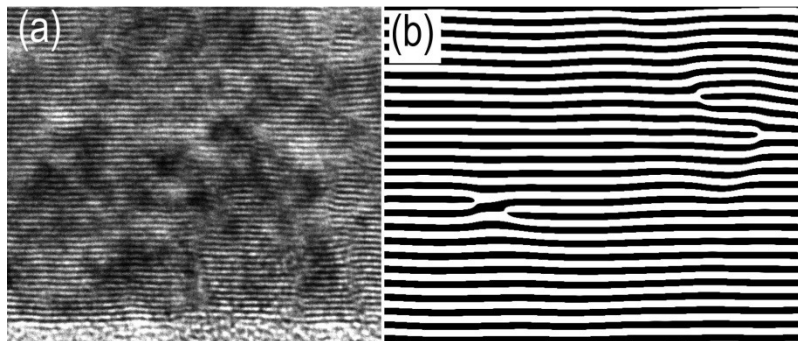

Fig. 4.   (a) Lattice image of 6.78 dpa irradiated NBG-18 and (b) noise-filtered magnified lattice image showing the prismatic dislocations dipoles. The spacing between two adjacent dark fringes corresponds to the (002) inter-planar spacing (~0.36 nm).

Publications

Refereed Journal Articles

J. Kane, C. Karthik, R. Ubic, W. Windes, and D. Butt, "*An oxygen transfer model for high purity graphite oxidation*," Carbon, 59 49-64 (2013).

C. Karthik, , J. Kane, D. P. Butt, W. Windes, and R. Ubic, "*Microstructural characterization of next-generation nuclear graphites,*" Microscopy and Microanalysis, 18 272-278 (2012).

J. Kane, C. Karthik, D. P. Butt, W. Windes, and R. Ubic, "*Microstructural characterization and pore structure analysis of nuclear graphite,*" Journal of Nuclear Materials, 415 [2] 189-197 (2011).

C. Karthik, J. Kane, D. P. Butt, W. Windes, and R. Ubic, "*In-situ transmission electron microscopy of the electron-beam damage process in nuclear grade graphite,*" Journal of Nuclear Materials, 412 [3] 321-326 (2011).

Refereed Conference Publications

J. Kane, C. Karthik, D.P. Butt, W.E. Windes, and R. Ubic, "*Oxidation studies on NBG-18 grade nuclear graphite,*" *Transactions of the American Nuclear Society, 105* 399-400 (2011).

J.J. Kane, "*Polycrystalline graphite oxidation: A simplified mechanistic approach,*" ANS Annual Meeting, Chicago, 24 – 28 June 2012.

Conference Presentations

J. Kane, C. Karthik, R. Ubic, D.P. Butt, and W. Windes, *"Microstructural characterization of next generation nuclear graphite,"* TMS Annual Meeting & Exhibition, San Diego, 27 February – 3 March 2011.

C. Karthik, J. Kane, D.P. Butt, W. Windes, and R. Ubic, "*In-situ TEM of electron-beam damage process in next-generation nuclear graphite,*" TMS Annual Meeting & Exhibition, San Diego, 27 February – 3 March 2011 (poster).

J. Kane, C. Karthik, W. Windes, D.P. Butt, and R. Ubic, "*Irradiation creep in nuclear graphite: Microstructural studies on non-irradiated graphite,*" 3rd Annual Very High Temperature Reactor (VHTR) R&D Technical Review Meeting, Denver, 27 – 29 April 2010 (poster).

J. Kane, C. Karthik, R. Ubic, D.P. Butt, M. Figueroa, and W. Windes, "*Microstructural characterization of next generation nuclear graphite,*" 11th International Nuclear Graphite Specialists' Meeting (INGSM-11), Eastbourne, United Kingdom, 12 – 15 September 2010.

C. Karthik, "*Microstructural characterization of nuclear graphites,*" 12th International Nuclear Graphite Specialists' Meeting (INGSM-12), Jeju, Korea, 20 – 23 September 2011.

J. Kane, C. Karthik, R. Ubic, D.P. Butt, and W.E. Windes, "*Oxidation studies on NBG-18 grade nuclear graphite*," <u>ANS Winter Meeting and Nuclear Technology Expo</u>, Washington, DC, 30 October – 3 November 2011.

J.J. Kane, C. Karthik, R. Ubic, W. Windes, and D.P. Butt, "*Oxidation study of a nuclear grade graphite*," <u>ANS Annual Meeting</u>, Chicago, 24 – 28 June 2012.

J.J. Kane, C. Karthik, R. Ubic, W.E. Windes, and, D.P. Butt, "*The graphite-oxygen reaction: A fundamental approach*," <u>13th International Nuclear Graphite Specialists' Meeting (INGSM-13)</u>, Meitingen, Germany, 23 – 26 September 2012.

J. Kane, C. Karthik, R. Ubic, W. Windes, and D.P. Butt, "*BX-ray CT:More than just an image*," <u>6th Annual Very High Temperature Reactor (VHTR) R&D Technical Review Meeting</u>, Idaho Falls, 7 – 9 May 2013 (poster).

J. Kane, C. Karthik, R. Ubic, W. Windes, and D.P. Butt, "*Graphite oxidation: An intrinsic approach*," <u>6th Annual Very High Temperature Reactor (VHTR) R&D Technical Review Meeting</u>, Idaho Falls, 7 – 9 May 2013 (poster).

J.J. Kane, C. Karthik, R. Ubic, W.E. Windes, and D.P. Butt, "*Nuclear graphite oxidation: The what, where, and why*," <u>14th International Nuclear Graphite Specialists' Meeting (INGSM-14)</u>, Seattle, 15 - 18 September 2013.